NTNU – Trondheim
Norwegian University of
Science and Technology

Toward Growth Control of (111)-oriented Perovskite Thin Films

La0.7Sr0.3MnO3/SrTiO3(111) a model study

Ingrid Gullikstad Hallsteinsen

Nanotechnology
Submission date: June 2012
Supervisor: Thomas Tybell, IET
Co-supervisor: Jos Boscker, IMTE

Norwegian University of Science and Technology
Department of Electronics and Telecommunications

Problem description

Over the last 20 years, advancement in physical deposition has led to the development of epitaxial all oxide systems, opening for combining epitaxially thin films of different crystalline oxides to form artificial materials. More recently it has become evident that interfaces between epitaxial thin films can carry functionality of its own. The most prominent example is the interface between $LaAlO_3$ and $SrTiO_3$ that is conducting, and can be both superconducting as well as magnetic. This is a rapidly growing research area, aiming at novel device technology based on such interface functionalities. However, one prerequisite is a high degree control of thin film surfaces and interfaces. Of special interest are interfaces between materials having different crystalline structure and orientation; however the development of such interface systems is a novel field.

The goal of this master thesis is to elucidate how pulsed laser deposition can be employed to control the surface properties of (111) oriented perovskites. In order for this the following two questions are to be addresses:

- Is it possible to develop (111)–oriented $(La, Sr)MnO_3/SrTiO_3$ heterostructures that have a controlled surface morphology?
- Can substrate treatment of (111)-oriented $SrTiO_3$ be employed to control the morphology of the thin films.

One sub-goal is also to elucidate on possible growth modes governing the synthesis of (111)-oriented $(La, Sr)MnO_3/SrTiO_3$ thin films.

Thomas Tybell
NTNU, Trondheim
June 15, 2012

Abstract

Control of growth and surface morphology of perovskite oxide thin films is essential for future electronic devices based on such materials. Uncommon crystallographic orientations, like (111), are particularly interesting in order to control domain formations, but have been shown to grow in a rough manner, because of their polar surfaces. This work aims to elucidate the growth mode of (111) oriented systems, to enable smooth surface structured films.

We have investigated the growth of $La_{0.7}Sr_{0.3}MnO_3$ (LSMO) thin films by pulsed laser deposition (PLD) on (111)oriented $SrTiO_3$ (STO), characterized by AFM and x-ray diffraction. Substrate surface preparation has been optimized to yield uniform straight step-and-terrace surface structures, as well as the ability to tune the surface structure by different surface preparations. The film surface structure is observed to duplicate the substrate surface; hence, control of the film surface structure is obtained.

A detailed description of the growth mode, from thin films of only a few mono layers to thick films of 70nm is presented. The growth mode is complex showing in principle an unstable growth. For the first 20 mono layers (2nm) a roughening transition from step-flow to layer-by-layer is observed. At higher thicknesses a second transition is seen, where the surface breaks up to a 3D surface structure. The critical thickness of the second transition is delayed by reducing the deposition temperature, as expected for strained surfaces, resulting in epitaxial thin films of step-and-terraces structure at least 70nm thick. The crystallinity of the films has been confirmed by XRD measurements. The transition to 3D growth is shown to initiate at the step-edges, and stabilizes with step-bunched steps. A speculative discussion of step-induced strain, and consequently the surface breakup is presented.

Furthermore magnetic measurements by VSM in room temperature are presented. The saturation magnetic moment is measured to be $330 emu/cm^3$ at room temperature, which is $100 emu/cm^3$ larger than other reported values for LSMO/STO(111) [1, 2].

The improved understanding of substrate preparation and growth mode in LSMO/STO(111) is important for further work on oxide interfaces, as we believe these results can be expanded to other (111) systems. The magnetic measurements give a preliminary indication that high quality films are necessary to exploit the full potential of these materials.

Sammendrag

Kontroll av vekst og overflate morfologi av perovskitt oksid tynnfilmer er essensielt for framtidige elektroniske enheter basert på slike materialer. Uvanlige krystallografiske retninger, som (111), er spesielt interessante for domene kontroll, men har blitt vist tidligere å vokse ujevnt, på grunn av den polare overflaten. Målet til dette arbeidet er å belyse vekstmoden til (111) orienterte materialsystemer, slik at filmer med glatte overflater blir mulig.

Vi har undersøkt veksten av $La_{0.7}Sr_{0.3}MnO_3$ (LSMO) tynn-filmer deponert ved hjelp av pulserende laser (PLD) på (111)orienterte $SrTiO_3$ (STO) substrat, karakterisert ved AFM og røntgen-diffraksjon. Overflatepreparering av substratene er optimalisert slik at uniforme rette stegkanter er oppnådd. I tillegg har studiene av overflatepreparering ført til muligheten til å regulere stegkantstrukturen til den ønskede strukturen. Overflatestrukturen til tynn-filmene duplikerer substratoverflaten eksakt, slik at kontroll av tynnfilm overflatestrukturer er muliggjort.

En detaljert beskrivelse av vekstmoden, fra monolags-tynne filmer til 70nm tykke filmer, presenteres. Vekstmoden er kompleks, og viser i prinsippet at veksten er ustabil. De første 20 monolagene (2nm) viser en ujevn vekst, hvor veksten går fra "step-flow" til lag-for-lag. For tykkere filmer er enda en vesktovergang er obsevert, hvor overflaten bryter opp til å bli ujevn og tredimensjonal vekst begynner. Veksten stabiliseres over tykkere filmer ved minkende temperatur, som forventet for filmer med spenninger, slik at steg-og-terrace strukturen er bevart til minst 70nm tykke filmer. Filmene er singel-krystalline, bekreftet av røngten-diffraksjon målinger. Overgangen til 3D vekst er vist å starte i stegkantene i overflatestrukturen, og veksten blir stabilisert ved høyere stegkanter. En spekulativ diskusjon av om spenninger og deformasjoner kan komme fra stegkantene i overflatestrukteren er presentert.

Magnetiske målinger gjort ved VSM i romtemperature er vist tilslutt. Det saturerte magnetiske momentet er målt til å være $330 emu/cm^3$ ved romtemperature, som er $100 emu/cm^3$ større enn andre rapporterte målinger for LSMO/STO(111) [1, 2].

Den forbedrede forståelsen av overflatepreparering av substrat og vekstmode i LSMO/STO(111) er viktig for videre arbeid innen oksid tynnfilmer, siden vi tror at disse resultatene kan utvides til andre (111)systemer. De magnetiske målingene gir en indikasjon på at høy kvalitet på tynn-filmene er nødvending for å utnytte the fulle potensialet for disse materialene.

Preface

The master thesis has been done at Institute of electronics and telecommunications, NTNU, spring 2012, as the final project in my Master of Science - Nanotechnology. The work is a continuation of my semester project [3], and is equivalent of 30ECT credits. The work was performed in the research group of electronic devices and materials, at laboratories of the institute and at NTNU Nanolab. In addition, TEM studies has been done by Magnus Nord at institute of physics, NTNU, and magnetic measurement has been done at University of Wisconsin, Madison by Thomas Tybell, Mark Rzchowski and Chang-Beom Eom.

XRD characterization is one of the most powerful tools to characterize thin films. Unfortunately, the XRD-machine has been out-of-order for ninety percent of my time at the institute. The XRD measurements in this study are therefor not as complete as could be expected. ϕ-scans where performed at University of Wisconsin, Madison by Thomas Tybell, Mark Rzchowski, S. Lee and Chang-Beom Eom, while reciprocal space maps where performed by Jos Bosckher at NTNU. I also want to mention Magnus Breivik, which has been helping out trying to get the XRD-machine running again.

I want to accord a special thanks to my supervisors Prof. Thomas Tybell and Jos Boschker. All honor to them, which has given me tremendous help at all times, motivating me and sharing their devotion to the field. Especially thanks for their patience during my numerous calls to their offices. I would also like to thank my parents for proofreading and valuable discussions, as well as my classmates for tips and tricks.

Ingrid Hallsteinsen
MTNANO
NTNU, Trondheim
June 15, 2012

Contents

Problem description . . . 1
Abstract . . . 3
Sammendrag . . . 5
Preface . . . 7

1 Introduction **11**
1.1 Motivation . . . 11
1.2 Background . . . 12
1.3 Outline . . . 12

2 Theory **15**
2.1 Transition metal oxide materials and the interface between them . . . 15
2.1.1 Symmetry and correlated electrons . . . 16
2.1.2 Strain . . . 17
2.1.3 Charge transport . . . 18
2.1.4 Magnetism . . . 20
2.1.5 Reconstructions at interface . . . 20
2.2 $La_{0.7}Sr_{0.3}MnO_3$ . . . 23
2.3 Thin film growth . . . 25
2.3.1 Thermal Equilibrium . . . 25
2.3.2 Kinetic approach . . . 26
2.3.3 Growth under strain . . . 28
2.3.4 The influence of surface structure on growth . . . 29
2.4 State of the art - LSMO/STO(111) thin films . . . 31
2.4.1 Substrate surface . . . 31
2.4.2 Growth mode . . . 31
2.4.3 Strain and structural reconstructions . . . 32
2.4.4 Magnetic measurements . . . 33

3 Experimental **35**
3.1 Preparation of substrates . . . 35
3.2 Pulsed Laser Deposition . . . 36
3.3 Reflection High-Energy Electron Diffraction . . . 37
3.4 Atomic Force Microscopy . . . 42
3.5 X-ray Diffraction . . . 43
3.6 TEM . . . 47
3.7 Vibrating Sample Magnetometer . . . 47

4 Results and Discussion **49**
4.1 Substrate surface . . . 49
4.1.1 Substrate preparation . . . 49
4.1.2 Crystallographic characterization of substrates . . . 52
4.1.3 Discussion . . . 54
4.2 Growth mode . . . 56

4.2.1 In situ measurements 56
4.2.2 Substrate influence on film growth 59
4.2.3 Temperature 60
4.2.4 Critical thickness 61
4.2.5 HF- substrates critical thickness 63
4.2.6 Crystal structure 65
4.2.7 Interface strain 68
4.2.8 Interface growth 69
4.2.9 Step bunching 71
4.2.10 Discussion 72
4.3 Magnetic properties 76
4.3.1 Magnetic analysis 76
4.3.2 Discussion 76

5 Conclusion and Further work **79**

1 Introduction

1.1 Motivation

Nobel laureate Herbert Kroemer's statement "The interface is the device" back in 2001 [4], referred to the astonishing success of semi conductor devices for the last 50 years. Eleven years later Nature Magazine [5] states that the claim still holds, and a new revolution of electronic devices is in sight: the appearance of oxide interface devices. Unlike semiconductors, perovskite transition metal oxides (TMOs) are interesting even in bulk form. Primarily the electronic state is highly correlated, leading to a wide range of properties such as magnetism, ferroelectricity, ionic conduction and superconductivity [6]. Secondly, the crystal structure is eminently adaptable to changes in composition, enabling doping and tuning of the physical properties [7]. Tuning of ordered properties, like ferromagnetism, are the basis for smart materials in devices [8]. Bringing interfaces, epitaxy and super lattices into the picture enable further control and enhancement of these properties, as well as new functionality. Possible applications of the one-going research are resistance random-access-memory (ReRAM), correlated solar cells, orbital-controlled transistor gates and manipulation of qubits by electric fields [5].

Oxide interfaces were traditionally far more difficult to grow than semiconductors, mainly for the same reasons they are interesting - the oxygen species and its polar nature [6]. As with the semiconductors, atomically abrupt interfaces, epitaxial growth and step-and terrace surfaces are required for device applications. Intense research the last two decades, has resulted in present oxide interfaces which rival the semiconductors in both crystallinity and abruptness [9]. This is largely achieved by 1) control of oxide substrate termination; 2) the use of pulsed laser deposition or molecular beam epitaxy and 3) the development of high pressure reflection high energy electron diffraction for monitoring [6]. At present the growth of oxides in the (001) direction is becoming a routine procedure, enabling detailed studies of interface effects. For instance, Li et al [10], have shown coexistence of magnetic order and two-dimensional superconductivity at the $LaALO_3/SrTiO_3$ interface, which earlier was believed to be mutually exclusive.

In Nature Magazines commentary of innovative oxide interfaces, [9], the growth of thin films in uncommon crystallographic directions, like the (111) orientation of cubic perovskites, is categorized as an important opportunity for enhanced control. Materials grown in this direction are expected to have strong structural and electronic coupling, as three corners of the oxygen octahedra are connected over the interface. New functionalities are therefore expected, such as artificial topological insulators or ordered ternary perovskites with novel cation arrangements [9]. In addition, control of growth in different orientations, makes us capable to tune domain formations in materials, as they are coupled to the crystal structure [11]. However, the (111) oriented surfaces present novel challenges during growth, as the substrate surface is polar; hence, research in this area is still in its infancy.

1.2 Background

We chose LSMO/STO(111) as a model system. The surface of (111) oriented STO has a hexagonal symmetry, and hence is symmetry matched with the $(001)_R$ plane of the rhombohedral oxide, LSMO. LSMO is a 100% spin polarized ferromagnetic half-metal, exhibiting T_c above room temperature and the colossal magneto resistance effect, making it promising for spintronic device applications [12]. The different crystallographic environment of a hexagonal structure is believed to modulate domain formations in the material, possibly leading to mono domains; hence, the magnetic moment and anisotropy of LSMO(111) are expected to deviate from LSMO(001) [13].

Control is the cue-word throughout this work. If control of growth of (111) surface is achieved, further control of properties is enabled, as well as the fundamental understanding of the correlated electronic state. Previously, I have done a semester project in the same field of research (see [3]). In the project, it was demonstrated that a prerequisite for surface control of films is surface control of the substrates. Furthermore, it was shown that step-and-terrace structured films are obtainable at decreased deposition temperature compared to optimal growth parameters of LSMO/STO(001). However, the surface morphology of relatively thick films where observed to be rough and three dimensional.

In order to enhance control of the growth, and elucidate the mechanisms behind the growth transitions, the emphasis of this work is the observed growth transitions of LSMO/STO(111). To enhance control of growth, an improved surface control is necessary. In this work an optimized control of substrate surfaces compared to the project is demonstrated, enabling engineered film surface structures. To understand the growth mechanisms I show how the surface morphology and epitaxial growth of the films evolve with thickness, resulting in a detailed description of the growth mode from interface to thick films of 70nm. The growth is demonstrated to be unstable in principle, possibly by accumulated step-induced strain. As well as growth properties, preliminary results of magnetic properties are discussed, showing promising results.

1.3 Outline

After this introduction, chapter 2 follows with a theoretical background of TMOs and thin film growth. To understand the motivation for oxide thin film research it is important to look closer at the materials in question. First, the electronic properties of an oxide interface are discussed, relating charge transport and magnetic properties to structure, strain and interface reconstruction. Second, a short description of LSMO is presented. In section 2.3 thin film growth is reviewed, describing different growth modes and how surface diffusion and strain contribute. Last the state of the art in (111) oriented thin films is reviewed, focusing on LSMO/STO(111).

The deposition and characterization methods are described in chapter 3: Experimental, where parameters are related to the theoretical growth modes described in the theoretical chapter.

The results are presented in chapter 4, which have been divided into three

sections; substrate surface (4.1), growth mode (4.2) and magnetic measurements (4.3). Each section is discussed independently. The pick of the basket is the growth mode, where each subsection represent a level of control, from substrate influence, temperature effects, the critical thickness, interface behavior and step-edge effects.

Finally, the conclusion and further work are presented in chapter 5.

2 Theory

The motivation to study oxide thin films lies with the future applications in electronic devices. To understand the opportunities and limits that arises, an understanding of the fundamental physics of oxide materials is necessary. In this chapter, the theoretical background of the materials is presented. The first section gives a detailed description of how the highly correlated state in transition metal oxides (TMOs) affect properties, and how these properties can be controlled. The discussion revolves around the degrees of freedom; charge, spin, orbital and lattice, discussing how the coupling between them can be explored and exploited. In this work $La_{0.7}Sr_{0.3}MnO_3$ (LSMO) has been used to investigate further the properties of TMOs. A short recap of the properties of LSMO is presented in section 2.2.

The second part is of a more technological character. To be able to realize thin film devices, control of the thin film growth is essential. Section 2.3 deals with the different theoretical models for thin film growth. Models are presented both for thermodynamic and kinetic growth, as well as for the influence of strain and directional step-edges on growth. As already mentioned in the introduction, different orientations can complicate the growth further. Finally in section 2.4, a survey of articles representing the state of the art in (111) oriented TMO thin film growth is presented.

2.1 Transition metal oxide materials and the interface between them

The heart of TMO materials is the complex correlation of spin, charge, orbital and lattice which enables control of the electronic functionality [6]. The coupled degrees of freedom give a conceptual control tool, as controlling one degree will control the rest and their associated properties. The coupling between the degrees of freedom is also responsible for inducing new properties such as high transition temperature superconductivity, metal-insulator transitions and colossal magnetoresistance [5]. In an article by Elbio Dagotto [14] TMOs are classified as complex matter because of its correlated state. The term "complex matter" are coined for biological materials; but several similarities can be found, such as complicated phase-diagrams, inhomogeneity at the nanoscale, degenerated states and the emergence of new behavior dominated by few rare events. Generally, TMOs have degenerated metastable states at the nanoscale which compete with each other, such that small perturbations in the environment; for example, external parameters as pressure or electric field, leads to large differences in the output properties [14].

The concepts explained in this section are generally applicable to all TMOs, but for simplicity the discussion will restrict itself to explaining them in the context of manganites of perovskite structure. Oxides have a dauntingly range of possible crystal structures available [6] with the commonality of ionic bonds, but the perovskite structure (chemical formula ABO_3) is the most common structure for research in TMOs [6]. Perovskites are simple, and their properties are tunable by cation exchange, making them perfect model systems.

2.1.1 Symmetry and correlated electrons

Hwang et al [5] show how the degrees of freedom and phenomena come together through the fundamental understanding of symmetry. As shown in figure 1 the electronic functionality of the oxide interface is described by how the coupling leads to ordered phenomena. The phenomena are directly related to the broken symmetry at the interface. Hwang recognizes three important symmetries for the order parameter; spatial inversion ($I : r \rightarrow -r$), time reversal ($T : t \rightarrow -t$) and Gauge symmetry ($G : G \rightarrow G+C$). Spatial inversion is clearly broken in all heterostructures - resulting in reconstructions of spin, charge and lattice. For insulating materials, a broken spatial inversion is linked to polarization and ferroelectricity. Time reversal symmetry corresponds to the complex conjugate of the wave vector; hence a reversal of time reverses the sense of phase and changes the sign of the spin operator. A break of time reversal symmetry then is usually associated with ferromagnetism. Gauge symmetry, which is a phase shift in the wave vector, is related to charge conservation, such that a broken gauge symmetry may induce superconductivity. In the middle of figure 1 "Emergent Electromagnetism" is placed. The coupling of all three degrees of freedom is predicted to form new phenomena yet unknown.

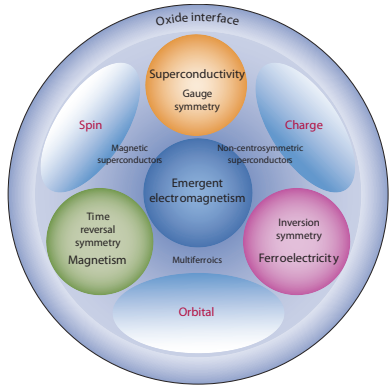

Figure 1: *Schematic of how the degrees of freedom, properties and symmetry are all coupled, leading to emergent electromagnetism. Reproduced from [5]*

To exploit the emergent phenomena of TMOs control of the interaction is essential. Figure 2 shows possible control parameters of an oxide interface. As mentioned in the beginning a control of one degree of freedom will lead to control of the coupling as well, leading to several fundamental control parameters. Control of the lattice is exemplified in figure 2a and b, either using lattice mismatch or different crystal structures to induce controlled strain in the material. The spin and orbital occupancy can be controlled by exchange mechanism between different electronic phases as shown in figure 2c as well as localization or quantum confinement of the electrons as shown in figure 2d. The charge and transport properties can be tuned by doping, i.e. changing the cations of the structure, as implied by figure 2e.

The entanglement of degrees of freedom also enables control by external sources

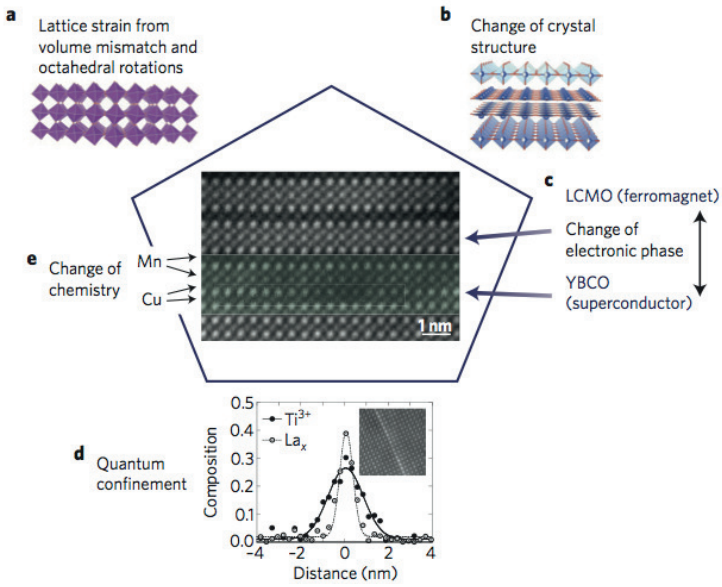

Figure 2: *Schematic of possible control parameters at a TMO interface. Centre panel: Scanning tunneling electron microscope image of an interface between* $La_{1-x}Ca_xMnO_3$ *and* $YBa_2Cu_3O_7$*. a) Elastic strain from volume mismatch and octahedral rotations. b) Symmetry and crystal structure. c) Change of electronic phase. d) Charge confinement. e) Change of chemical bonding and valence state. Reproduced from [9]*

[6]. In magneto electric materials the ordered magnetic structure is coupled to the polarization, so that a switch in polarization, for example by an external electric field, induces a change in the magnetic easy axis. For applications in electronic devices the magneto electric coupling is especially interesting, where control of magnetic structure by external electric power minimizes the energy consumption of the device [15].

2.1.2 Strain

Mayhap the most important control parameter for thin film growth of TMOs is epitaxial strain. Homogeneous strain comes from the mismatch of lattice parameters over the interface. Selective choice of substrate and film materials, leads to control of the lattice mismatch and thereby the induced strain. Experimentally one has found that induced strain changes the transition temperature of superconductivity, ferroelectricity and spontaneous magnetization; hence a control of strain is a control of properties. Strain often lead to structural reconstructions. In perovskites the structure may reconstruct using oxygen rotations, Jahn Teller effect or changing the metal-oxygen bond angle and length [16]. These reconstruction change the electronic environment explaining the change in electronic properties.

A more detailed look at manganites, show several general couplings between

strain and magnetic properties, some of which are shown in figure 3. An increased distortion results in an increase in magnetic anisotropy, making thin films having higher anisotropy than bulk. Looking at the lattice parameters in-plane with the surface, an elongation leads to positive magnetic anisotropy, while in-plane compression leads to negative magnetic anisotropy. It is also demonstrated that for most cases a tensile strain leads to a magnetic easy plane which is in-plane with the surface, while compression of the unit cell leads to magnetic easy axis which is out-of-plane from the surface. The curie temperature (T_c) is shown to increase with compression, because of the increased hopping probability. A tensile stress on the other hand decreases T_c as the $Mn - O$ bond is stretched, and hopping becomes unfavorable. The Jahn Teller distortion is found to increase the band gap of the material, as well resulting in a decrease of T_c. [17]

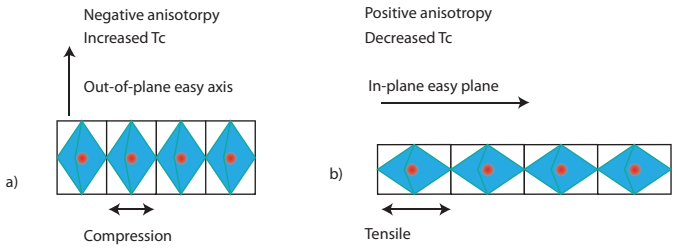

Figure 3: *Schematic of different strain and resulting magnetic properties; a) compressive strain b) tensile strain. The blue represents the oxygen octhahedra, the red circle the manganese ion, the black square the perovskite unit cell.*

2.1.3 Charge transport

Undoped TMOs are generally Mott insulators, indicating the highly correlated state. In Mott insulators the traditional band picture would predict a metallic behavior, but taking into account the interaction between electrons, an insulating state is found, where the electrons are localized to each lattice site [18]. In TMOs, the d-electrons determine the electronic properties [5]. The d-orbitals in transition metals are localized; hence, the distance between electrons is smaller and the Coulomb interaction becomes more dominant than in regular metals. The perovskite structure and its electronic configuration are shown in figure 4a. The octahedra of oxygens around the transition metal produces a crystal field of cubic symmetry and split the degenerated 3d orbitals of the transition metal into two degenerate states; t_{2g} (xy, yz, and zx orbitals) and e_g ($x^2 - y^2$ and z^2 orbitals). Transport properties are determined from the double-exchange mechanism (explained in [3]), using the p-orbitals of the oxygen as an intermediate hopping state. The transport is then highly dependent on direction, as the s-orbital of the transition metal and the p-orbital of the oxygen must have a non-zero orbital integral overlap. Figure 4b shows that for hopping over an interface in the xy-plane, three possible configurations are possible.

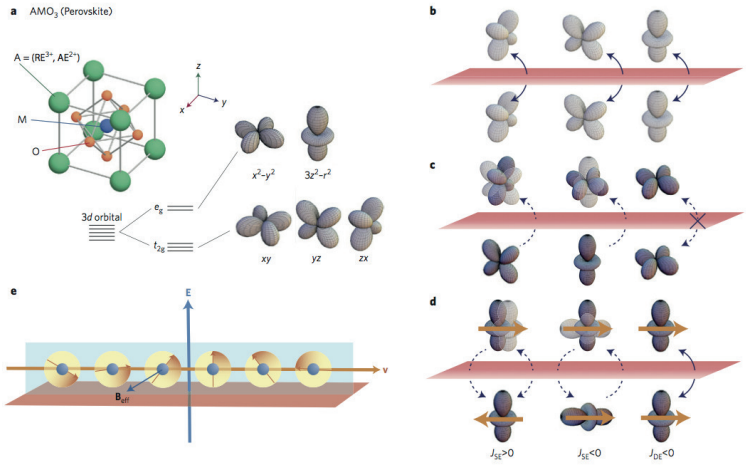

Figure 4: *Orbital and spin configurations at interfaces. a) Perovskite structure and orbital energy levels under the cubic crystal field due to oxygen ions. b) Allowed hopping between orbitals across the x-y interface. c) Allowed virtual hopping across the interface. The lightly colored orbitals are the destination of the virtual hopping process, while the electron is occupied in the darkly colored orbital. d) Various exchange interactions across the interface ($J > 0$, antiferromagnetic; $J < 0$, ferromagnetic); left, antiferromagnetic super-exchange interaction (J_{SE}) using the same orbital in the intermediate state; middle, ferromagnetic super-exchange interaction between different orbitals; right, double-exchange interaction (J_{DE}) where the real hopping of the conduction electron between the two M ions mediates the ferromagnetic coupling. e) Rashba-type spin–orbit interaction. Reproduced from ref. [5]*

The correlation exchange between the d-orbital electrons is determined by virtual hopping, which mediates a super-exchange mechanism [5]. Virtual hopping is a quantum mechanical process by which an electron can "tunnel" through the region separating neighboring lattice sites and join its neighbor, only for the electron or its neighbor to hop back a moment later. The likelihood of this happening is governed by the relative orientations of the spins of the electrons [19]. The electron correlation leads to a constraint on the number of electrons at a given site in the TMO; hence, the degrees of freedom, like charge, spin, orbital and lattice are locally entangled as already mentioned[20]. For virtual hopping, as well as real electron transfer, only some hops are possible due to symmetry. Figure 4c show two allowed hops, and one forbidden for the same xy-plane.

In the perovskite structure it is possible to engineer physical properties by substituting the cationic species, i.e controlling the charge by doping. This leads to mixed-valence states. The cations are placed in the A and B sites of the perovskite, respectively in and around an oxygen octahedra. Doping changes the fill factor of the d-orbital, contributes an extra spin to the magnetic structure, and may also result in distortions in the crystal symmetry which changes the bandwidth of the material [6]. Both electron and hole-doping are possible, and the result of the

(hole)doping differs if the holes are created in the d-band or the 2p-band. In manganites, the mixed valence state consists of Mn^{3+} and Mn^{4+}. Only Mn^{3+} experiences Jahn Teller distortions, which impose a tetragonal component to the cubic crystal field. The distortion of the whole crystal is therefor dependent on the doping factor, as well as the electronic properties.

The macroscopic charge transfer over doped TMO interfaces is not easily described through band-diagrams. Doping, exchange mechanisms and correlation effects all contribute to create complex phase-diagrams of the band profiles. The complexity induces unexpected phenomena at the interface. An example is the $SrTiO_3/LaTiO_3$ interface introduced in the introduction, where $SrTiO_3$ is a band insulator, $LaTiO_3$ is a Mott insulator, while the interface is metallic due to charge transfer from $LaTiO_3$ to the empty d-orbitals of $SrTiO_3$ [7].

2.1.4 Magnetism

Both super-exchange and double-exchange mechanisms are highly coupled to the magnetic state; the double-exchange mechanism favors ferromagnetic order, while super-exchange can lead to both ferro and anti-ferro magnetic order depending on orbital filling and directionality. In figure 4d, three allowed mechanisms for the xy-plane is depicted, where the super-exchange interaction, J_{SE}, is positive for antiferromagnetic materials and negative for ferromagnetic materials. The two first hops are of virtual hopping character, while the last is an example of the double-exchange interaction, J_{DE}.

The exchange mechanisms are different for the different ionizations. The $Mn^{4+} - O - Mn^{4+}$ super-exchange leads to an antiferromagnetic state, while $Mn^{3+} - O - Mn^{3+}$ can lead to both ferro and anti ferromagnetism. The $Mn^{4+} - O - Mn^{3+}$ mediates charge transport trough the double exchange mechanism, and results in a ferromagnetic state. In such a state the degeneracy between $Mn^{4+} - O - Mn^{4+}$ and $Mn^{3+} - O - Mn^{3+}$ is lifted. All three mechanisms compete in a complex magnetic phase diagram.

The broken spatial inversion at an interface may lead to a spin precession in the plane. As seen in figure 4e for a xy-interface a Rashba spin-orbit coupling in the yz-plane occurs.

2.1.5 Reconstructions at interface

As well as charge transfer, the electrostatic boundary conditions of the interface play an important role for interface reconstructions [21]. For an interface between two perovskites of different polarity a polar discontinuity occurs. The large energy cost of atomically abrupt interfaces in a hetero-structure between planes of different polarity results in reconstruction. If there is no reconstruction at such an interface, there will be an electric field which diverges with thickness over the interface, as shown in figure 5 [7]. To avoid this situation there are two possible outcomes; atomic or electronic reconstruction. The reconstruction of atomic structure and intermixing of ions over the interface is usually not wanted, resulting in non-abrupt interfaces, but spatial continuous change. On the other hand

the redistribution of electrons stabilizes the interface. The mixed valence charge compensation reflects the ability of TMOs to hold different valences [22]. Though there is still an active debate on the different polar stabilization processes in interfaces, a clear constraint on all of the bound and free charges of the system is set by the electrostatic boundary conditions, and equilibrated with respect to the electrochemical potential.

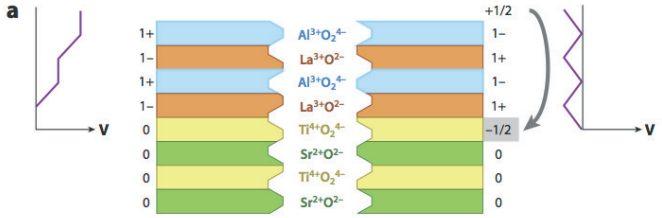

Figure 5: *Electronic reconstruction of the $LaAlO_3/SrTiO_3$ surface.The polar discontinuity between the two materials results in a potential build-up across the $LaAlO_3$ layer (left). To avoid the internal electric field an electronic reconstruction occurs, bringing electrons to the $LaAlO_3/SrTiO_3$ interface to screen the internal field. Figure reproduces from [7]*

Spin-orbital reconstructions at the interface are often associated with the atomic and electronic reconstructions already described above. A modulation of charge results in polarization of the spin-orbit interaction, while epitaxial strain results in rotations of the oxygen octahedra, which changes the crystal field and the preferential orbital occupation. For a different orientation of the surface, for example the (111) oriented surface three corners of the oxygen octahedra instead of one are connected across the interface. This additional interaction is expected to result in strong structural and electronic couplings and reconstruction. In addition the interface itself may directly induce orbital reconstructions as the crystalline environment found just a unit cell away from the interface is fundamentally different, as seen in figure 43 [5].

In conclusion Clearly control of reconstructions at interface is essential to control properties. Selective choice of substrate and film and epitaxial growth controls the internal strain, while doping level determines the stoichiometry at the surface, and the electronic phases of both surfaces determine the exchange mechanisms. The electrostatic boundaries are determined by the surface termination. Epitaxial growth, surface stoichiometry and termination are therefor essential in further advanced towards applications.

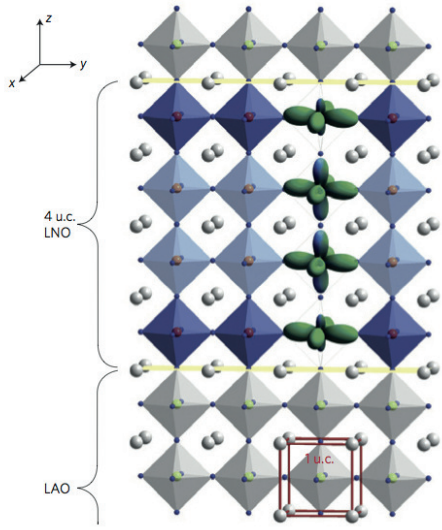

Figure 6: *Heterostructure of metallic $LaNiO_3$ with partially occupied Ni e_g orbitals (LNO, blue) and insulating $LaAlO_3$ (LAO, white). Only one unit cell away the electronic environment is different from the environment at interface. Figure reproduced from [5]*

2.2 $La_{0.7}Sr_{0.3}MnO_3$

In this section, a short review of the material properties of $La_{0.7}Sr_{0.3}MnO_3$ (LSMO) is included. A more thorough explanation of origin of the physical properties and effects can be found in previous work [3].

LSMO has a distorted perovskite structure, with a pseudo-cubic lattice parameter of $a_{pc} = 3.871$Å (rhombohedral $a_r = 5.471$Å and $\alpha_r = 60.43°$). [23, 24]. The distortion is a compression along the (111) axis of the unit cell, making LSMO rhombohedral with point group $R\bar{3}c$ [12] and the tolerance factor of LSMO is $t = 0.9$ [25]. In this work, all crystallographic indices are in the pseudo-cubic reference. The distortion is due to oxygen octahedra rotation and Jahn Teller distortions. In addition, LSMO is valence-mixed, both Mn^{3+} and Mn^{4+} exist, an effect which is due to the doping of Sr in the material. The electronic configuration of Mn^{3+} is $1s^2 2s^2 2p^6 3s^2 3p^6 3d^4$, where the d-orbital is split due to crystal field and Jahn Teller effect, resulting in the orbital occupancy shown in figure 7.

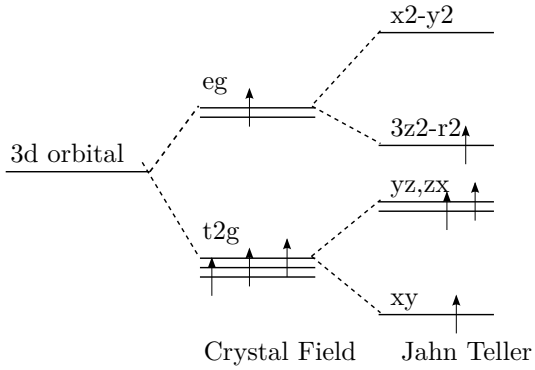

Figure 7: *The 3d-orbitals in LSMO splits first in two (e_g and t_{2g}) due to crystal field splitting, and then into four ($x^2 - y^2$, $z^2 - r^3$, yz/xz and xy) due to the Jahn Teller distortion. The orbitals are only occupied by one type of spin leading to ferromagnetism.*

The Fermi level of the material is determined by the hybridization of the spin up e_g orbital in Mn and the p orbitals of oxygen, which results in a band gap between the spin up and down orbitals, with the Fermi level in between. LSMO is therefore a 100% spin polarized material [12]. LSMO is ferromagnetic at room temperature (300K) at doping levels between $0.2 < x < 0.5$ and antiferromagnetic for other doping levels [6]. The ferromagnetic phase is due to the double exchange mechanism between the manganese-atom, which also induces high mobility, while the paramagnetic phase will suppress charge transport. A metal-insulator transition (T_{MI}) is therefor observed around T_C, though the Jahn Teller effect induces a small discrepancy between T_{MI} and T_C [12, 26].

The magnetic easy axis in bulk LSMO is found to be in the (111) plane in the pseudo cubic lattice, as a consequence of the rhombohedral distortion, resulting in eight possible magnetic domain formations [27]. For thin films of LSMO/STO,(001)

several authors have found that the magnetization relaxes at surface to become in-plane with the surface [28]. But, also out-of-plane components are found, believed to be at the domain walls of the in-plane components, which are determined by steps at the surface [29]. For epitaxial films, it has also been shown that the elastic domains (and indirectly the stress) contribute to the determination of the magnetic domains. The curie temperature of LSMO(001) is found to be 370K and the saturation magnetization at room temperature is around $300 - 400 emu/cm^3$ [2]. Magnetic anisotropy is found to change with the temperature. Between T_c and $250K$ for a (001)oriented film, the $< 100 >$ and $< 110 >$ axis are equivalent easy axis, while below the $< 110 >$ is easier than the $< 100 >$ axis. [17]

2.3 Thin film growth

Thin film growth is a non-equilibrium kinetic process where a material condensates into a thin film on top of a substrate [30]. To be able to characterize the process, and understand the underlaying mechanisms different models for thin film growth are presented. The discussion is restricted to epitaxial growth, which refers to the growth of a single crystal specifically oriented to match the substrate. An ideal film would grow epitaxially in a layer-by-layer fashion, forming an atomically abrupt interface while maintaining the bulk stoichiometry.

Thin film growth contain several processes on the atomic level, which can be categorized into absorbtion, surface diffusion, nucleation and growth [30], as shown in figure 8.

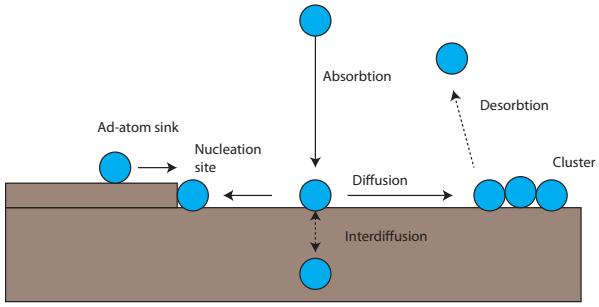

Figure 8: *Schematic of the growth process; ad-atoms arrive at surface, are absorbed, diffuse across the surface or into the material, nucleate into clusters or desorb into the ambient again.*

During absorbtion, the ad-atoms arrive at the surface with a certain flux and form a bond with the substrate atoms. The type of bond depends on the interaction between the ad-atoms and the substrate, and after a time the ad-atoms may desorb into the ambient. The ad-atoms diffuse along the surface, or inter-diffuse into the material, before settling/nucleating. Steps in the surface can act as nucleation sites, ad-atom sinks or energy-barriers for diffusion. During surface transport ad-atoms collides, forming clusters, which may nucleate into stable islands. After some time, a saturation density of stable islands is reached; where it is more probable for an ad-atom to join an existing island than nucleate a new. This is growth. The type of growth can either be two-dimensional, where islands of only one monolayer coalesce or three-dimensional where the islands grow at several layers simultaneously.

2.3.1 Thermal Equilibrium

From the sketched scenario, clearly thin film growth rates are dependent on the rates of absorption, bonding, diffusion and nucleation, making the process kinetic in character. However, a consideration of minimization of energy is beneficial to categorize the growth as the growth can be in local equilibrium.

The energy to form an interface ($\Delta\gamma$) consist mainly of two terms; the energy

due to formation of a surface of both materials and the interaction between the two (γ_i);

$$\Delta\gamma = \gamma_{film} + \gamma_i - \gamma_{substrate} \tag{1}$$

The sign of $\Delta\gamma$ result in three different growth modes; named Frank - van der Merve, Volmer-Weber and Stranski-Krastinov [31], which are drawn schematically in figure 9.

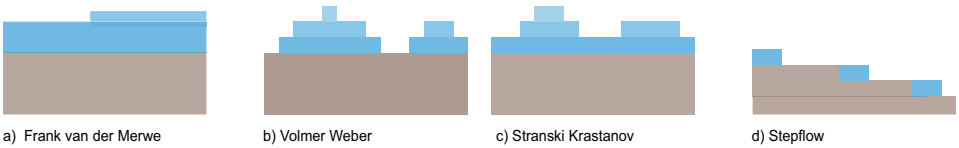

Figure 9: *Schematic of the four growth modes. a) Frank van der Merve - layer by layer, b) Volmer Weber -island c) Stranski Krastanov- layer to island and d) Step-flow. The different blue colors represent different layers of the film.*

In Frank - van der Merve mode a 2D layer-by-layer growth is observed, where one monolayer is finished before starting a new layer. In this case $\Delta\gamma < 0$, or $\gamma_{film} + \gamma_i < \gamma_{substrate}$ [30], i.e. this mode is characterized by a more beneficial interaction between substrate and ad-atom than between the ad-atoms [6]. As the surface energy of the film and interface must be less than the substrate, the larger the substrate surface energy, the easier layer-by-layer growth is achieved.

On the other hand for Volmer-Weber growth, ad-atom interaction is more favorable and island growth is observed. In Volmer-Weber growth the criterion is opposite ($\Delta\gamma > 0$). A large film surface energy will be reduced most efficiently by the coming ad-atoms to reside on top of the already present atoms, instead of the substrate [6]. The result is a 3D surface topography, consisting of islands as seen in figure 9 b.

For Stranski-Krastinov growth the growth starts as a layer-by-layer-growth, but at a critical thickness becomes island-growth. The transformation from 2D to 3D growth is associated with mass transport along the surface. A strained film will accumulate strain energy, increasing the interface energy for each layer. At the critical thickness, the interface energy will be sufficiently large that the term $\gamma_A + \gamma_I$ is larger than the substrate energy. Then, the growth will transform from 2D to 3D growth, as the ad-atoms favors the film sites to minimize the total energy. It has been observed that for some systems, 3D islands are situated only along certain crystallographic axis, indicating strong island-island interaction. Stranksi-Krastinov growth mode may also originate in a change in the chemical potentials or symmetry during growth.

2.3.2 Kinetic approach

The modes above are all considerations from an equilibrium point of view, but thin film growth is a kinetic process, so surface diffusion should be a part of the picture [30]. For simplicity, a consideration of homo-epitaxy is beneficial. For

homo-epitaxy there is no strain, and from an equilibrium point of view the growth would be layer-by-layer. Other effects are therefor solely kinetic. Two different processes can be found, the diffusion across a flat terrace called *intra*layer mass transport and the diffusion across a step-edge onto a lower terrace called *inter*layer mass transport. The step-edge is an energy-barrier to the diffusion of ad-atoms. Diffusion to an upper terrace is neglected, as the energy-barrier is too high to overcome, while diffusion to a lower terrace is possible through interlayer mass transport. Interlayer mass transport therefor needs higher energy than intralayer mass transport.

Looking at the earlier defined growth modes in this aspect, we see that island growth must be dominated by intralayer transport. The ad-atoms diffuse across the terrace, not across any step-edges, and nucleate mainly on the island where they are absorbed. In layer-by-layer growth; however, the atoms drop down into the steps between the islands, without nucleating on top of terraces, indicating domination of interlayer transport. The competition between intra and interlayer transport depends on diffusion length vs terrace width and the step-edge barrier.

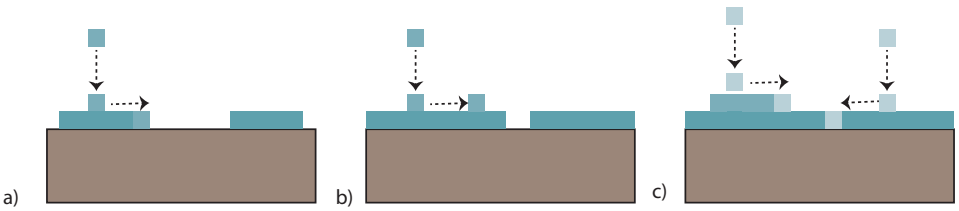

Figure 10: *Schematic of layer-by-layer growth with second nucleation. a) island short enough to continue growth b) second-layer nucleation c) nucleation and coalesce*

In real life an ideal layer-by-layer growth is never achieved, second-layer nucleation always happens before the first layer is finished. A schematic of the growth is shown in figure 10. When second-layer nucleation starts, the distance an ad-atom deposited on top of an island to reach the edge is less than the diffusion length. The ad-atoms will therefor contribute to growth, instead of nucleating new islands as seen in figure 10a. As the islands starts coalesce, the distance to the step-edge gets longer than the average nucleation distance, and it is more likely that the ad-atoms start nucleating on the terrace instead, as illustrated in figure 10c. The continued growth consists of both coalescence and nucleation as seen in figure 10c. To obtain 2D growth it is therefor beneficial to have a high coverage before coalescence. It is therefor more beneficial to categorize the growth modes in the critical coverage at second-layer nucleation, θ_c, and the coverage when coalescence initiates θ_{coax}, instead. This means that;

$$\theta_c > \theta_{coax} \tag{2}$$

cause 2D, layer-by-layer growth and

$$\theta_c < \theta_{coax} \tag{3}$$

cause 3D, islands growth. An important conclusion can be made from this discussion concerning process parameters. A transition from 3D to layer-by-layer 2D growth can be achieved by augmenting the critical coverage. This can be achieved by increasing the temperature, which will increase the diffusion across step-edges and the critical coverage. The opposite is true for decreasing the depositing rate [30].

Another relevant type of growth where surface diffusion determines growth is step-flow growth (figure 9) In reality no substrate is atomically flat, so all substrates can be treated in a step-terrace manner. In this growth mode the atoms nucleate at the lower terrace adjacent to a step, where they coalesce into new steps. It would seem like the steps only move forward as more material is deposited. A possible effect of step-flow growth is meandering edges instead of straight edges [32]. The mode is determined by intralayer mass transport, the ad-atoms diffuse across the terrace and the edges act as sinks, such that all nucleation happens at the step. To achieve step-flow growth the terrace-widths must be shorter than the mean diffusion lengths, such that the ad-atom condensation will predominantly be at steps instead of terraces. Step-flow growth can also lead to step-bunching, which leads to a gradual decrease of step-density. Step-bunching is also seen by increasing growth temperatures, or annealing temperatures, as the diffusivity of the surface species increases with temperature.

2.3.3 Growth under strain

Including strain into the discussion, adding a competing elastic energy to the surface energies, makes several important differences in the growth theory. In heteroepitaxy a certain lattice mismatch exists between substrate and film; hence, the film is strained as the film has the same structure as the substrate in-plane [6]. The lattice mismatch can be defined as:

$$f = \frac{a_{film} - a_{sub}}{a_{sub}} \tag{4}$$

where both lattice parameters are in the surface plane. To minimize the strain of the film this quantity should be held as small as possible. If $a_{film} < a_{substrate}$ the film will be in tension, otherwise in compression. Strain energy accumulates with film thickness and may result in misfit dislocations, film buckling or a transformation from 2D to 3D growth as already discussed, depending on growth kinetics and the relative energetics of the processes [30].

At a certain critical film thickness (T_c), the film may relax to bulk parameters. Van der Merwe examined the case of a uniformly strained over-layer and determined that with a strain less than a critical value, the energy of the over-layer was less than the energy of an array of dislocations necessary to relax the film. From this it was concluded that strained films grow in registry with the substrate until reaching a critical thickness, where dislocations appear [33]. The process is shown in figure 11a and b.

A kinetic approach predicts a second critical thickness of stability ($T_c(k)$ (figure 11), which is determined by the substrate interaction range over the film. At this

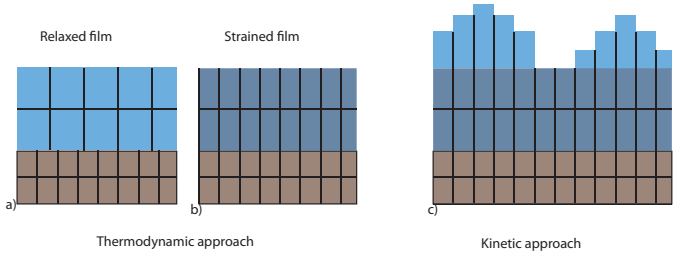

Figure 11: *Schematic of a film grown epitaxially on a substrate, with a lattice mismatch, under thermal equilibrium and with kinetic considerations. a) The film relaxes to bulk parameters through dislocations at interface, b) The film is strained, keeping the substrate lattice parameters c) The film transforms to 3D growth after the kinetic critical thickness without dislocations. The crystal structure is drawn as black lines.*

critical thickness the growth transforms from 2D to 3D, without dislocations. It is found that a decrease in temperature suppresses the instability, increasing the critical thickness.

Sander et al [33] show that for a strained state, which is kinetically stable ($T < T_c(k)$) the growth is similar to the layer-by-layer growth described earlier with 2D island which coalesce (figure 9), but rougher. For low strain the growth is characterized by large islands with small gaps between them, while higher strains leads to smaller islands and larger gaps. The borders between the islands are at points where the local strain energy competes with the bond energy. In this case it is seen that a large diffusion length leads to possible nucleation of new islands, while short diffusion lengths leads to coalescence. A long diffusion length lets the atoms travel to the preferential sites, leading the ad-atoms away from the strain-associated gaps. A low mobility on the other hand hinders this process, and the atoms are constrained to the gaps. For thin film growth which are strained it is therefor better to lower the growth temperature to obtain a smoother growth by shortening the diffusion length, and increasing the critical thickness.

Yang and Srolovitz [34] show how an original smooth elastically stressed surface can evolve into a crack-like surface, confirming the instability of strained surfaces. Using a sinusoidal surface they show that the maximum strain energy density occurs at the "valleys" of the surface (see figure 12). When a hole is made in the surface, matter diffuse away from this position and the groove deepens rapidly with continued growth, while matter accumulate at the side of the groove, resulting in 3D surface. The crack is made without dislocations, but act as a pathway of nucleation of dislocations.

2.3.4 The influence of surface structure on growth

Several authors conclude that the step-and-terrace structure is determining for the growth evolution, though the exact influence varies from article to article. Huang et al [35] show that for Gd-doped ceria thin films step edges introduce strain, as

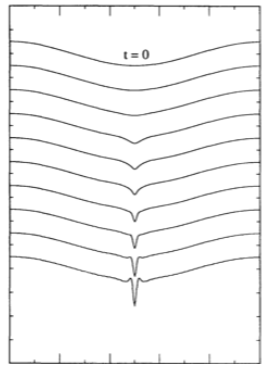

Figure 12: *Schematic of the evolution of a crack in the surface. Reproduced from [34]*

the height of the unit cell in the growth direction is different from film to substrate. The height difference leads to reconstruction of the unit cell exactly at step-edge - which propagates along specific planes with film growth, and can be seen by TEM and HRTEM as strain. Sanchez et al [36, 37] has investigated the growth transition from step-and-terrace to 3D surfaces of manganites (001). He shows that the transition starts with 2D islands and holes. The holes are observed to be at the step-edges, but no explanation is provided. The islands coalesce with the upper terraces, and meandering steps are seen, before nucleation on top of the islands leads to a 3D surface of islands and "wedding cake" or pyramidal islands are obtained. The nucleation is seen to be at the edges of the islands, which are explained by an energy-barrier to cross into the lower terrace, stabilizing the cluster.

In conclusion clearly control of the substrate surface is essential to control growth. The imposed strain on the film by substrate, the surface step-edges and the surface energy all profoundly modulate the growth.

2.4 State of the art - LSMO/STO(111) thin films

Not much work has been done at (111)oriented TMO surfaces, but the field is emergent, new articles being published as we speak. To the author's knowledge, this collective review of work contains all relevant previous research.

2.4.1 Substrate surface

According to Blok et al [38] there are three criteria for a good substrate surface; single termination, stable interface with air and stable interface with the deposited film. For (001) orientations, the only possibility is polar films deposited on top of neutral substrates. However, the unavoidable surface reconstruction seems not to have sever impact, as it is shown with coherent epitaxial growth. On the other hand will (110) orientations have problems with procuring single terminations and stable interfaces with air, as the substrate will be polar. This obstacle can be overcome by growing a thin layer of oxygen depleted substrate. The excess charge at the interface is then compensated by oxygen vacancies, and no reconstruction or intermixing is observed. The (111) orientation suffers difficulties from all three of the above criteria. The surface reconstruction prevents coherent growth at the first few mono layers, and the polar discontinuity leads to intermixing and electron movement of multivalent metals [38].

Previous work on LSMO growth on STO(100) concludes that control of substrate surface structure is essential for film growth, where the desired structure is a step-and-terrace structure of atomically defined step-heights of one unit cell and uniform straight terraces. In the (111) direction of STO the distance between equivalent planes is $0.23nm$, and the symmetry is quasi-hexagonal/3-fold. Several methods of surface preparation have been reported for the STO(111) with various result. Duan et al [39] reported etching with $HCl : HNO_3$ at different times and annealing temperatures, resulting in straight step-edges, but not single termination. Several reports [40, 41] show better results with buffered HF with single-terminated atomically sharp steps, while Chang et al [41] shows almost as good results with only etching in DI-water.

A few studies have been done looking at the termination and relaxation of the STO(111) interface, where the two possible terminations are SrO_3^{4-} and Ti^{4+}.Tanaka et al [42] found that at annealing of 1180° the SrO_3 surface was the terminating surface, while for annealing at 1220° the surface where terminated by Ti^{4+}. At the intermediate 1200° both terminations where found, and following step-heights of half a unit cell. Sigmund et al [43] on the other hand found only Ti^{4+}-terminations when annealing at 950°. In this study there where not steps of one unit cell, but multiple unit cells per step indicating step bunching. Haruyama et al [44] also found the surface structure varying with annealing temperature, where higher temperatures resulted in higher Ti^{4+} content.

2.4.2 Growth mode

The growth mode and roughness for different orientations are believed to be different because of the different terminations possible. For LSMO the termination in

the (111) orientation is; $LaSrO_3^{3.3-}$ and $Mn^{3.3+}$, and it is therefore a polar discontinuity for the (111) interface of STO/LSMO. It has been seen by several authors that substrates of (111) STO and accordingly films are found to be rougher than for the (100) direction because of the increased polarity. Blok et al[38] has shown that the polar discontinuity at the (111) interface can be avoided by metallic screening. In the case of $BiFeO_3$ on $SrTiO_3$, the material almost immediately grows in a 3D growth mode if it is grown directly on the $SrTiO_3$. The reconstructed polar surface seems to restrain the wetting of the film material on the substrate. However, Blok shows that if it is grown with a conducting buffer layer of $SrRuO_3$, it grows in a 2D growth mode. The explanation for the coherent growth can be given by the excess charge screening that the buffer layers provide.

D. Rubi et al [45] has looked at the surface morphology for $SrRuO_3$ at (111)STO at different thicknesses, and seem to find a growth which initially is island growth, then coalescence into 2D atomic flat terraces before a new roughening stage is found. At thin films of 6nm the growth is rough, but as the growth continues the valleys are filled with material, forming flat terraces, which also is recorded by 2D RHEED images at around 20nm. For thicknesses around 40-50nm the 3D island growth starts again.

Chang et al [46] show how growth mode at the initial growth depend on growth parameters for $SrRuO_3$ at (111)STO. At deposition temperatures of $700°C$ and growth rate of 0.074 unit cells/s, similar growth as reported by Rubi et al [45] is shown, going from smooth 2D to rough 3D and back to smooth 2D for the first nine monolayers. The roughening at thin films is attributed to the polar reconstruction to suppress then increase of electric potential with thickness. Increasing the temperature to $800°C$ however, extends the first layer-by-layer growth to 9ML, but then a rougher, undefined growth is observed. Increasing the growth rate to 0.222 unit cells/s for the high temperature case resulted in a growth which resembled the low temperature case; while decreasing the growth rate to 0.019 unit cells/s for the low temperature case results in growth which resembles the high temperature case. Increased growth rate is then observed to lead to coalescence of clusters into mono layers, while decreased growth rate results in second-layer nucleation and triangular surface forms.

2.4.3 Strain and structural reconstructions

Structurally for a (100) orientation of STO the distortion of the LSMO film is tetragonal, while the (111) orientation undergoes trigonal distortions. The out-of-plane strain should therefore differ for different orientations. But, Chopedekar et al [2] show a converging out-of-plane parameter to $3.84 - 3.86$Å for (100), (110) and (111) surfaces, indicating the same strain. Yongsheng et al[47] has examined LSMO(111) growth on top of LAO(111), and finds a negative out-of-plane strain of 0.4% to the (111) orientation, compared to a positive 1% to the(100), (110) orientations, and explains the fact with a lager elastic modulus of the (111) orientation which should result in smaller disorder at the interface. They also report smoother films at (111) orientation, but the AFM images reveal 3D growth for all orientations, making smoothness a difficult parameter.

Lepetit et al [48] has proposed a model to predict the interface effects in LSMO/STO(001). This model has its basis in making an energy balance for the different contributions, assuming an equilibrium state. They propose three different constraints at the interface. Firstly, the substrate parameters constrain the film parameters, such that $a = a_{STO}, b = b_{STO}$. This elastic energy is relatively strong, associated with bond lengths, and relaxes slowly, just after around 1000 Å. The second constraint is the films in-plane symmetry, which is also imposed by the substrate. The associated energy is weak, acting on bond angles and relaxes at just a few mono layers. Finally, the electronic structure also interacts over the interface.

For LSMO/STO(001) the tensile stress favors a contraction of the c-parameter in the film, while the electronic interaction favors an elongation. This is explained as delocalization of Mn e_g electrons into the empty 3d Ti orbitals, because of the polar discontinuity. The result is a Jahn Teller distortion to increase the d_z^2 occupation, hence, an elongation. Lepetit [48] has calculated the electronic energy to be two orders of magnitude larger than the elastic energy, resulting in an elongation of the c-parameter at the first mono layers, then relaxes to a compression. This is verified by experimental observations, where the c- parameter is elongated at the first three mono layers. This change of structure also changes the magnetic and transport properties. In these three first mono layers the d_z^2 occupation is dominant over $d_x^2 - z^2$ which decreases the double exchange, and therefor reduces the curie temperature and the conductivity.

For LSMO/STO(111) the tensile stress is the same, favoring a contraction. The polar discontinuity however is smaller, but still there is a charge difference of 0.7. If electrons flow into the substrate, both z^2 and $x^2 - y^2$ orbitals will contribute to the reconstruction. To counteract and increase the occupation an elongation in the growth direction is favorable. If one assumes the strength of the interaction is still stronger than the tensile stress, an analogous but weaker reconstruction at the surface is obtained. Just contemplating the unit cell, implies that a further tilting of the unit-cell would also increase the occupation.

2.4.4 Magnetic measurements

It is also shown that different orientations will lead to different magnetic domains [49]. For a cleavage at the (111) surface the symmetry will no longer be cubic, but hexagonal. This may lead to new magnetic domains in the films, like vortex or radial structures, or single-domain structures.

One of the few studies of LSMO/STO (111) has been done by Chopdekar et al [2], which compares magnetic measurements as a function of film thickness for different orientations, the (100), (110) and (111) orientations respectively. Their results show that for films with (110) and (111) orientation the magnetism is not reduced substantially at interface, while the (100) orientation showed large suppression of the magnetic moment for films less than 20nm. Chopdekar et al argue that the more polar surfaces of (110) and (111) are more susceptible to strain relaxation, which allows for quicker recovery of the spin moment as a function of thickness than the (100) orientation.

Gibert et al [50] recently showed that (111) super lattices of $LaNiO_3$ and $LaMnO_3$ on top of STO(111) substrates, yielded magnetic exchange bias at low temperature, indicating large interactions between the paramagnetic $LaNiO_3$ and the ferromagnetic $LaMnO_3$. The interaction has not been seen for similar super lattices in the $< 001 >$ direction, confirming the larger interaction at 111.

Several authors [1, 2] show a saturation magnetic moment of $200 emu/cc$ for LSMO/STO(111) at room temperature.

In conclusion it appears that the increased interaction exhibited by (111) oriented surfaces may lead to new ways for interface-engineering of properties. However, still many technical issues related to growth remains, requiring further research.

3 Experimental

In this chapter the experimental setup and experiments are explained, including the preparation of samples, the use of the pulsed laser deposition (PLD) and the characterization of the resulting thin films. Several techniques were used for characterization: atomic force microscopy (AFM), reflected high energy electron diffraction (RHEED), x-ray diffraction (XRD) and transmission electron microscopy (TEM). The different instruments are explained with emphasis on application to study oxide thin film growth, with all relevant parameters given.

3.1 Preparation of substrates

$SrTiO_3(111)$ substrates with a size of $10 \times 10mm$, one-side polish and a $0.1° \pm 0.1°$ miscut where used for all experiments. The substrates where etched and annealed to form single terminated surfaces with uniform step-edges before deposition.

The project thesis [3] resulted in a standard procedure; submerging the substrates for 5 minutes in Acetone, 5 minutes in Ethanol and 30 minutes in deionized (DI) water under ultrasound sonication. The DI-water was heated to $70°C$ before sonication, and the ultrasound-bath where put in heating mode. DI-water was used as a selective etching chemical as the complex $Sr(OH)_2$ is solvable in water, and the solvability increases exponentially with temperature. The procedure is therefor thought to result in a selective etch of Sr at elevated temperatures, resulting in TiO_2 termination [51, 41]. The volume of DI-water used was $40 - 80mL$. To evaporate all residues of the chemical solvents and define, the surface structure the substrates were annealed in a furnace oven under constant oxygen flow. Optimal time and temperature have been found in previous work [3]; two hours at $1200°C$.

In this work, a second preparation method was investigated as a compliment to the standard procedure. This method uses buffered hydrogenfluorid (HF) as additional etching chemical. Buffered HF has previously been shown to be effective by different authors [41, 40], resulting in unit-cell step-heights and straight well-defined terraces. The substrates were submerged in acetone, ethanol and DI-water under sonication, as in the standard procedure, but only for 5 minutes each, before dipping in buffered HF. The solution was 1:7 $HF : HNO_3$ with a pH of 4.7. The dipping time was varied between 1s, 30s and 45s. To stop the HF-etch, the substrates where rinsed for 5 minutes in DI-water. Post-annealing where done at temperatures of 1050° and 1150° for one hour and 1200° for two hours.

Both preparation methods have been used for film growth throughout this work. All substrates where cut in four equal pieces by a diamond cutter, at 75 grams and 100rpm. The cut where done after the pretreatment to ensure that the substrates did not flip over under sonication, hindering the etching process - as the substrates have only one-side polish.

Before deposition the substrates where cleaned once more with 5 minutes in acetone and 5 minutes in ethanol under ultrasound sonication and dried with Nitrogen gas. Then the substrates where glued to the sample holder with silver paste. The sample holder and substrate where then annealed for better adhesion and thermal contact for 1 hour at a hot plate of $150°C$.

3.2 Pulsed Laser Deposition

Pulsed laser deposition (PLD) is a deposition technique, utilizing non equilibrium laser-matter interaction, with the possibility of stoichiometric material transfers [6, 52]. Advantages of PLD are, effective diffusivity regime at low temperature, high adhesion between ad-atoms and substrate, epitaxial growth and promotion of the nucleation rate due to supersaturation and tunable repetition rate [6]. The setup and main physical phenomena are explained in previous work [3]. Below a more detailed description of how parameters affect growth of oxide thin films are presented.

In PLD the deposition rate and the degree of supersaturation are high, such that generally one approximates instantaneous deposition. The time of a laser pulse in PLD is generally shorter than the diffusion time, creating a separation in time between deposition and diffusion. In the time-interval between pulses, the high density of ad-atom clusters diffuses and nucleate to larger structures. To have epitaxial growth, the ad-atoms must have sufficient kinetic energy to diffuse across the surface. The kinetic energy of the ad-atoms when they reach the surface can be tuned by tuning different parameters.

The initial kinetic energy is determined by the energy of the laser. The laser pulse heats the target material with a sudden local increase in temperature, which in turn leads to instantaneous vaporization of the target species. The atoms ionize to a plasma with high kinetic energy as they absorb the remaining energy of the laser pulse. The high-energy ions are then transferred to the substrate by strongly forward-directed expansion, where the driving force is the large pressure gradient, forming a plasma plume. During the expansion, multiple collision with the ambient pressure occurs and the kinetic energy is reduced. After a certain traveling length, L, the atoms are in thermal equilibrium with the ambient, called the thermalization length. The plasma plume and the thermalization length are shown in figure 13.

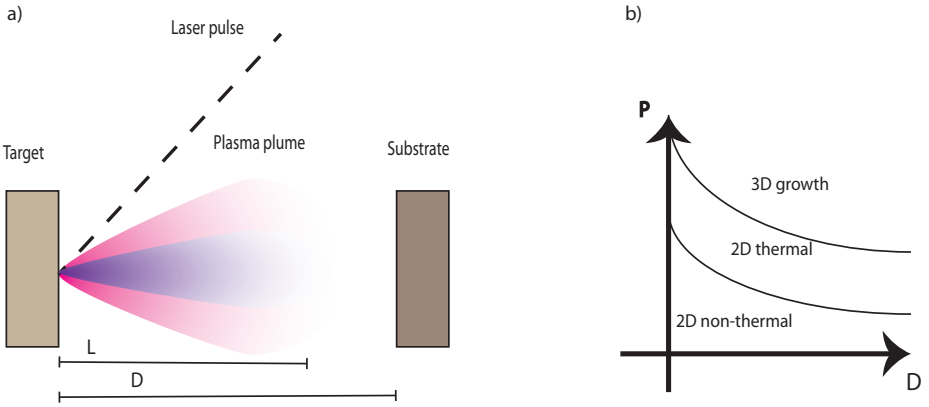

Figure 13: *A schematic of growth by PLD. a) The pink plume is the small laser area, purple is the large laser area b) the growth modes as a function of pressure and target - substrate distance.*

The attenuation of kinetic energy is determined by the interaction between the ad-atoms and the ambient, which can be controlled by the pressure, P, and the substrate - target distance, D. A shock wave equation of the form $PD^3 = constant$ describes the relation between them at a specific value of the kinetic energy. An increase in pressure will lead the expansion of the plasma to slow down, which will reduce the kinetic energy of the ad-atoms. The substrate-target distance naturally behaves in the same way, an increase leads to larger degree of thermalization and reduced energy [17].

Boschker et al [53] work on growing LSMO/STO(001) films show that by increasing the pressure the growth goes trough several transitions, from non-thermal 2D growth to thermal 2D growth and finally rough 3D growth as shown in figure 13. Both thermal and non-thermal grown films experience a roughening transition with deposited time. The transition occurs faster for non-thermal growth than thermal growth and is explained by preferential resputtering of the cations. Preferential resputtering is in accordance with the experimental data, as the amount of resputtering will increase for high-energy ad-atoms compared to thermal ad-atoms. The resputtering changes the cation stoichiometry, decreasing the amount of Mn in the film.

Using LSMO/STO(001) structures Song et al [54] show that a change of the laser spot area changes the cation stoichiometry as well. An increase in area changes the ratio between the A-site cations (La and Sr) and the B-site cation (Mn) from a significant A-site excess to a slight deficiency. This can be understood by considering the evolution of the plasma plume with area. For small areas, a bright and broadly divergent plume was observed, ablating material over a wide solid angle perpendicular from the target. With increasing laser area, the plume is increasingly focused to the substrate direction, diminishing the differences in the angular distribution of the cations, thus improving cation stoichiometry. The two different plume expansions are shown schematically in figure 13. The laser spot area can therefor be used to control cation stoichiometry.

In this project the PLD parameters where set to obtain 2D thermal growth, commencing with optimal parameters for LSMO/STO(001). A KrF excimer laser of 248 nm was used, at 21-24kV and 1Hz. The chamber was held at a pressure 0.35 mbar 100% oxygen, and temperatures were varied between 500° C and 750° C. The target-substrate distance was held at 45 mm. After the deposition, the samples were cooled down to room temperature in 100 mbar oxygen ambient at a rate of $15°/min$.

3.3 Reflection High-Energy Electron Diffraction

For in situ characterization of the thin film growth Reflection High-Energy Electron Diffraction (RHEED) was used. The measured intensity is an $in-situ$ measure of the roughness of the film surface; hence, it can be used to determine the growth mode [52]. A detailed description of the instrument setup and physical explanations is found in previous work [3], while this section reviews some of the finer details using RHEED as a characterization method for oxide thin film growth.

The diffraction pattern itself gives an indication of surface structure, where

a circular pattern indicate 2D-surfaces, while rectangular patterns indicate 3D surfaces, as seen in figure 14. A diffuse pattern indicates rougher surface than a sharp pattern [52].

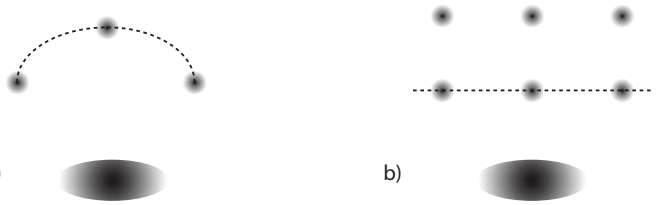

Figure 14: *Schematic of the diffraction peaks for RHEED, for a) 2D surface and b) 3D surface*

If the growth is ideal layer-by-layer, an oscillation pattern of intensity as a function of time is found, where one period from peak to peak relates to the growth of one monolayer. For an ideal growth the maximum of the peaks will be constant, maintaining a smooth topography of the film, as shown in figure 15a. The intensity oscillations come from the increased diffuse scattering at the edge of ad-atom clusters. The periodic formation of such edges by nucleation and coalescence of islands leads to an oscillation of cluster- edge density reflected in the RHEED oscillation. As a cluster-edge increases the diffuse scattering, it is the minimum RHEED intensity that corresponds to the maximum cluster-edge density. Assuming equally spaced islands and growth by step propagation, the cluster-edge density oscillation can be described by:

$$S = 2\sqrt{\pi N_s}(1-\theta)\sqrt{-ln(1-\theta)} \tag{5}$$

where N_s is the number of nuclei per unit area and θ is the surface coverage [55]. This function corresponds to measured observations, but does not consider destructive interference of the scattered beams. It was recently shown [56] that specular RHEED signals are affected by the destructive interference from electrons scattered from different layers. To model the RHEED signals considering destructive interference one can use the anti-Bragg x-ray intensity dependence of coverage, which is caused by such destructive interference: [57]

$$I(t) \propto (\frac{1}{2} - \theta_0 - \sigma_0 + 2\sum_m \sigma_m e^{-k_m t})^2 \tag{6}$$

where θ_0 is the coverage before a pulse is deposited, σ_0 the coverage corresponding to a single pulse, σ_m the amount of interlayer transport and k_m the rate constant. As RHEED intensities also depend on destructive interference, this model can be used to explain the intensity profile in RHEED measurements.

In growth by PLD, one can assume instantaneous deposition under the laser pulse, and subsequent time-interval for nucleation and diffusion of the ad-atoms. In singular surfaces a large initial decrease followed by a relaxation of the change in intensity is seen in this time frame, as shown in figure 15b. The initial decrease

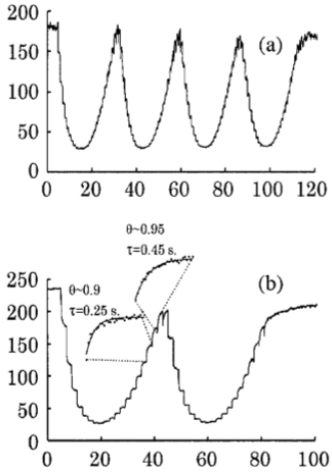

Figure 15: *Simulated RHEED intensity by the step-density model. a) ideal layer by layer growth b) the change in intensity first decreases rapidly, then relaxes. The relaxation is dependent on the coverage. Reproduced from [55]*

is explained by the deposition of ad-atoms acting as a high density of scattering points, before diffusion and nucleation starts. Using the step-density model the following relaxation is explained by diffusion of ad-atoms which attach into already existing islands, thereby decaying the density of diffusing species and step-edges. If one ignore second layer nucleation the decay time has an exponential decrease with coverage increase. For second layer nucleation on the other hands, the decay time is different depending on if the step is located on top of an island or between islands. The relaxation dependence on the coverage is then more complicated, where increased coverage will lead to a decay time which a) increases on top of islands and b) decreases between islands.

Using the interlayer mass transport model and the destructive interference, the roughness of a surface will modulate the RHEED signal, as the amount of interlayer mass transport depends on the ratio between ad-atom diffusion length and the length scale of surface roughness. In this model an ideally flat surface will show a continuing decrease of RHEED intensity after the pulse, instead of the relaxation found in the step-density model. The RHEED intensity and proposed diffusion model is depicted in figure 16. As only a small amount of the ad-atoms can arrive on top of layer two, the majority will diffuse into layer two and become scattering points for destructive interference - decreasing the intensity further. For a surface of more than half filled coverage, the intensity will increase as the ad-atoms diffuse into the holes of layer two. This is in accordance with the step-density model. For a similar coverage but larger surface roughness the increase will be even larger.

Boschker et al [58] showed a qualitative way of determining the roughness from RHEED. Using equation 6, the equation were simplified for almost full coverage and normalized into

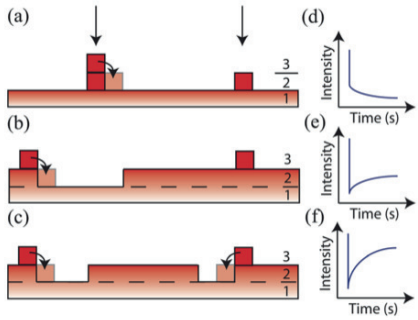

Figure 16: *Schematic of the interlayer mass transport model. a)-c) show schematic of the growth d)-f) show the corresponding RHEED intensities. Reproduced from [58]*

$$I(t) = \Delta I(1 - e^{-k_1 t}) \tag{7}$$

where ΔI is the relative change in intensity during the measurement. The numerical value of ΔI is found to be larger for rougher samples grown under thermal conditions than samples grown under non-thermal conditions. Throughout the growth it is also found that for the rough sample ΔI remain constant for several layers, while for the smooth sample it is increasing, indicating a surface roughening transition. All of which is consistent with characterization by other means, which makes ΔI a reliable parameter for roughness characterization.

In step-flow growth of vicinal surfaces the resulting RHEED signal is constant, as the step-edge density is almost constant throughout the growth. For a transition between layer-by-layer and step-flow, the RHEED-signal will change from oscillating to constant and can be used to approximate the diffusion length of the ad-atoms. The transition can be made by changing the vicinity (terrace width) or the temperature (diffusion length), as the width of the terraces must be approximately the same as the length of diffusion for such a transition to occur. But also mixed growth can lead to constant RHEED signal, so the method is not completely reliable [55].

The RHEED oscillations are dependent on growth parameters as well. It has been shown that in PLD growth the oscillation amplitude is decreased by an increase in kinetic energy, as the ad-atoms diffusion length increases. Song et al [54] growing LSMO/STO(001) using the laser spot area to change the kinetic energy, show the process by stopping the deposition at a RHEED minimum (maximum roughness), as shown in figure 17. In this case increasing the kinetic energy results in better growth, but the RHEED signal is worse. In conclusion the optimal RHEED oscillations are not always observed for optimal film growth conditions, but rather for high energy ad-atoms.

In this work RHEED patterns and intensity profiles, where taken for each deposition. The samples where rotated to acquire the highest possible intensities, however, no reproducible oscillations where obtained. It is believed to be a cause

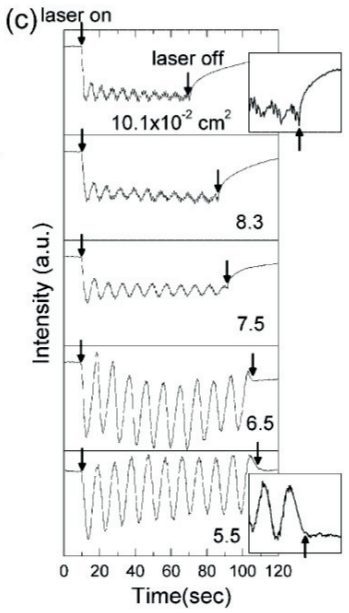

Figure 17: *The difference in RHEED signals as a function of laser spot area. The laser spot area is decreasing with each consecutive figure, while the RHEED signals are increasing in intensity with each consecutive figure. Reproduced from [54]*

of non-ideal PLD parameters for RHEED, but further work is required.

3.4 Atomic Force Microscopy

Atomic Force Microscopy (AFM) is a surface technique to image the topography with nanometer precision. The technique is explained and discussed in my previous work [3]. The microscope has been used under tapping mode for all experiments, and all post-analyses of the images are done in the Gwyddion software.

In figure 18 a clarification of expressions to describe the surface structure are schematically depicted. "Step-and-terrace" structure is used generally about a surface structure consisting of defined steps and terraces of any size. For steps of one unit-cell height, "atomically defined" is used, while steps of more than 3 unit-cells are called "step-bunched". "Uniform" steps refer to a sample with the same step-heights and widths at all measuring points. The height of one unit cell is also called a monolayer. Generally, the surface is categorized after the step-heights instead of step-widths as the heights are more precise in an AFM and observed to be more uniform. The shape or form of the steps is categorized as meandering, faceted or straight as seen in figure 18b. The 3D forms seen are illustrated in figure 18c, as "wedding cakes" and "fingers".

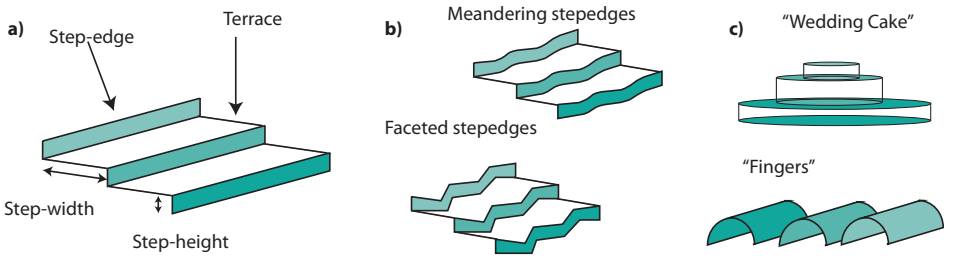

Figure 18: *Schematic of the step-and-terrace structure. a) step-width and step-height b) meandering and faceted step-edges c) observed 3D forms: "wedding cake" and "fingers"*

3.5 X-ray Diffraction

X-ray diffraction (XRD) is an analytic technique exploiting the scattering of x-rays to determine the crystallographic structure of a material. The wavelength of x-rays is comparable to the interatomic distance; hence, they are ideally suited for probing the structural arrangement of atoms. In this section the fundamental physics of XRD is covered, as well as the different methods for characterization of thin films.

Several x-ray - electron scattering processes occur, but it is the elastic scattering, i.e. scattering with conservation of energy, which is used for measurements in diffraction experiments. Diffracted waves from different atoms interfere with each other, and the resultant intensity distribution is strongly modulated by this interaction. If the atoms are arranged in a periodic fashion, as in crystals, the diffracted waves will consist of sharp interference maxima (peaks) with the same symmetry as the distribution of atoms. Measuring the diffraction pattern therefore allows us to deduce the distribution of atoms in a material. [59]

A schematic of the XRD process is depicted in figure 19. The incoming x-ray photon is characterized by the wave vector $\bar{K}_0$, the exiting x-ray photon by $\bar{K}$. The scattering by the scattering vector $\Delta\bar{K}$, which is defined as $\Delta\bar{K} = \bar{K} - \bar{K}_0$. The change in direction is denoted by the angle 2θ.

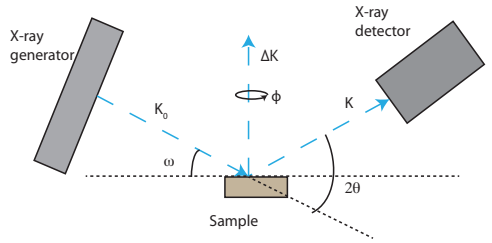

Figure 19: *Schematic setup of XRD. The incoming x-ray beams ($\bar{K}_0$) hits the sample with an angle ω, and the diffracted beam $\bar{K}$ leaves the sample with an angle 2θ from the incoming beam.*

The difference in phase factor between beams scattered at points separated by a distance d is $exp[-i\Delta\bar{K}d]$. The amplitude of the scattered wave is proportional to the local electron concentration, $n(\bar{r})$, at the point of scattering $\bar{r}$, hence the total amplitude of the scattered wave is given by:

$$F = \int dV n(\bar{r}) exp(-\Delta\bar{K} \times d) = \sum_G \int dV n_G exp[i(\bar{G} - \Delta\bar{K}) \times r] \tag{8}$$

where the Fourier components of $n(\bar{r})$ is used, and $\bar{G}$ is the set of reciprocal lattice vectors, such that $n(\bar{r})$ is invariant under all crystal translations. From equation **??** it is clear that the maximum amplitude is given by:

$$\Delta\bar{K} = \bar{G} \tag{9}$$

Equation **??** is a statement of the Bragg condition, which can also be stated as:

$$2d_{hkl}sin\theta = \lambda \tag{10}$$

where λ is the wavelength of the x-ray, θ the scattering angle, and d_{hkl} is the spacing between parallel lattice planes that are normal to the direction $\bar{G}$, such that $d_{hkl} = \frac{2\pi}{|\bar{G}|}$. In figure 20, both equations (equation 9 and 10) for the Bragg condition are shown geometrically. In figure 20a the crystal is represented as reciprocal scattering points. To produce constructive interference, the scattering must be of a certain angle θ such that the difference in incoming and outgoing beam $(\Delta\bar{K})$ is equal the distance between two reciprocal points. In figure 20b the crystal is represented with atomic planes of distance d. Here constructive interference happens when the difference in travel-length is equal to an integral number of the wavelength. The travel length between the two beams are $2dsin\theta$. Measurable intensities of XRD occur when there is constructive interference. Both equation 9 and 10 show that constructive interference occurs at certain angles of θ, which are dependent on the crystal structure.

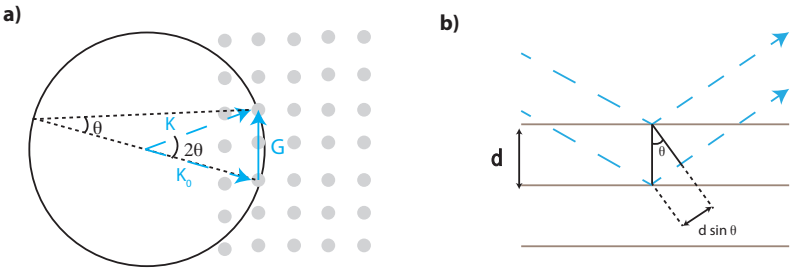

Figure 20: *Schematic of the Bragg condition. a) Reciprocal space: x-ray wave vector $\bar{K}_0$ terminates at a reciprocal lattice point, and a diffracted beam will be formed if the difference between them is the reciprocal vector $\bar{G}$. b) Real space: x-ray beams scatter at atomic planes with distance d and constructive interference is possible for certain angles, when the difference in traveling length is equal to an integral number of the wavelength. The circle is a representation of the Ewald sphere. All points that intersect with this sphere will have fulfilled the Bragg condition.*

Using the kinematically approach the intensity of a x-ray wave scattered by a crystal can be approximated to be [60];

$$I = |A_{crystal}|^2 = \frac{sin^2(N\Delta K\alpha/2)}{sin^2(\Delta K\alpha/2)} \tag{11}$$

where N is the number of scattering planes and α is the lattice vector. Figure 41 show representation of such an intensity graph for N=10. The major peaks are separated with a distance 2π, while the number of peaks reflects N as the distance between them are $2\pi/N$. For the limit of a thick sample with many scattering planes (N large) this function transforms into a series of delta functions centered at multiples of 2π, such that thick samples reflect only the major peaks. On the other hand if one would only consider a free standing monolayer; namely, N=1,

equation 11 gives $I = 1$. This would mean that the diffraction from the monolayer will be independent of $\Delta\vec{K}$ and will take on a finite, constant value.

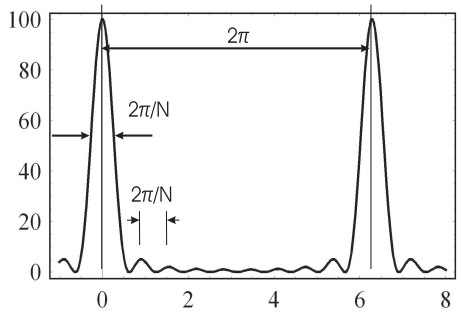

Figure 21: *Simulation of equation 11 at N=10 reconstructed from [60].*

Generally speaking thin film diffraction refers not to a specific technique but rather a collection of XRD techniques used to characterize thin film samples grown on substrates [59]. Basic XRD measurements made on thin film samples include:

- $\theta - 2\theta$ scans
- Rocking curve measurements
- Superlattice measurements
- ϕ scans
- Glancing incidence x-ray reflectivity measurements
- Texture measurements
- Reciprocal space mapping

In $\theta - 2\theta$ scans the incoming x-ray angle is θ, while the detector is placed at angle 2θ with respect the incoming x-ray beam, as in figure 19. During measurements, the x-ray source is fixed while the sample and the detector are rotated so that the configuration $\theta - 2\theta$ is preserved. As can be seen in figure 19 this constrains the scattering vector ΔK to the same direction as the normal of the surface, which means that only planes parallel to the surface are measured in the scan. For a wide angular range the scan can give an idea about the preferred orientation of the film. For good epitaxial growth only one particular type of plane (hkl) are observed, the preferentially oriented planes with the substrate plane.

Epitaxial films are extremely thin in comparison with the penetration depth of X- rays, hence, an intense peak as a result of the diffraction from the substrate will always be visible in $\theta - 2\theta$ scans. For hetero-structured films, the film peak will be observed shifted a distance from the substrate peak. The shift is a measure of the discrepancy in out-of-plane lattice parameter for substrate and film.

Generally the width of the peaks increases with decreasing thickness of the sample. But, determination of the thickness by width measurements is not trivial as other effects also lead to a broadening of the peak; for example, strain in the material. [61]

As already seen in equation 11 and figure 19b intensity maxima corresponding to constructive interference and minima due to destructive interference are recorded. The position of these features is directly related to the thickness of the layers and called "thickness fringes" [61]. A simple fit from equation 11 gives an accurate measurement of the thickness of the film.

Rocking curves are made without the constraining coupling between ω and θ. In this scan, the detector arm is fixed (fixed 2θ) while the sample is rotated (changing ω) to detect the reflection from planes with the same (hkl) indices which are in slightly different orientations. The sharpness of the peak then indicates the crystalline perfection. The full-width half-maximum (FWHM) can be used for comparisons, for example between substrate and film. [60]

To determine the symmetry of the sample ϕ-scans is made. In ϕ-scans the sample is rotated in-plane, as seen in figure 19, so the scan measures at which orientation the different crystallographic axis can be found.

Reciprocal space maps are a contour mapping of the distribution of intensity in the vicinity of the Bragg peak, resulting in a two dimensional map of diffracted X-ray intensity as a function of position in the reciprocal space. The reciprocal space map data are collected by repeatedly taking $\omega - 2\theta$ scans with the position of the detector being varied from the exact Bragg angle. Reciprocal space maps have the advantage that the lattice misfit and degree of lattice relaxation can be obtained independent of the miscut of the diffracting lattice plane with respect to the surface. In a $h - k$ scan, the in-plane or lateral lattice misfit appears as a separation between substrate and film peaks along h or k directions. If the h-l scan or k-l scan is taken, the difference in out of plane lattice parameter can be measured as the peak separation of substrate and film peals along l direction [62].

The transformation of the recorded angles (2θ and ω) to $K_\perp$ and $K_\parallel$ is done using the following simple transformations:

$$K_\perp = \Delta K \times cos(\delta) \tag{12}$$

$$K_\parallel = \Delta K \times sin(\delta) \tag{13}$$

where $\delta = \theta - \omega$ is called the offset and $\Delta K = 2K_0 \times sin(\theta)$. [63] Reciprocal space maps are plotted as a function of reciprocal lattice parameters instead of real lattice parameters, where

$$q_x = \frac{1}{d_x} \tag{14}$$

$$q_z = \frac{1}{d_z} \tag{15}$$

In this work $\theta - 2\theta$ scans, ϕ scans, rocking curves and reciprocal space maps have been utilized. Thickness fringes have been used to determine the thickness of the samples. Reciprocal $h - l$ maps have been used determine the in-plane lattice misfit between the substrate and film. The reciprocal space maps have been done by Jos Boschker. The ϕ-scans where done by Thomas Tybell, Mark Rzchowski, S. Lee and Chang-Beom Eom at the University of Wisconsin - Madison.

3.6 TEM

Transmission Electron Microscope (TEM) has been used to characterize the crystallinity, lattice parameters, thickness and strain of the films. The TEM sample preparation and imaging where done by Magnus Nord at NTNU.

3.7 Vibrating Sample Magnetometer

A vibrating sample magnetometer (VSM) measures the DC magnetic moment as a function of many parameters, obtaining hysteresis loops, thermomagnetic analysis, anisotropy, and magnetization as a function of time. It has a flexible design and combines high sensitivity with easy of sample mounting and exchange at any operating temperature. Powders, bulk and thin films are all possible material samples [64]. This section explains the general physical basis of the instrument and its use for thin films.

The principle of VSM, by the detection of the magnetic moment induced in a coil of wire, is based on Faraday's law of induction;

$$\epsilon = -N\frac{d}{dt}(BAcos\theta) \tag{16}$$

where N is the number of turns in the coil, A is the coil turn area and θ is the angle between the B field and the normal to to the coil surface. A schematic of the experimental setup is found in figure 22. The sample is fixed to a sample-holder inside a uniform magnetic field, such that the sample is magnetized. The sample is then physically vibrated sinusoidally along the Z-axis perpendicular to the magnetizing field by an electromechanical transducer. Pick-up coils are mounted in close proximation to the sample and the oscillatory motion of the magnetized sample induces a voltage in the pickup coils. The output electric signal has the same frequency of vibration, and its amplitude will be proportional to the magnetic moment of the sample, amplitude, and relative position with respect to the pickup coils system. However, since it is also proportional to the vibration amplitude and frequency, the moment readings taken simple by measuring the amplitude of the signal are subject to errors due to variations in the amplitude and frequency of vibration. In order to avoid this difficulty, a nulling technique is frequently employed to obtain moment readings that are free of these sources of error. These techniques make use of a vibrating capacitor for generating a reference signal that varies with moment, vibration amplitude, and vibration frequency in the same manner as the signal from the pickup coils. When these two signals are processed appropriately, it is possible to eliminate the effects of vibration amplitude and

frequency shifts. In that case one obtains readings that vary only with the moment of the sample. [65, 66]w

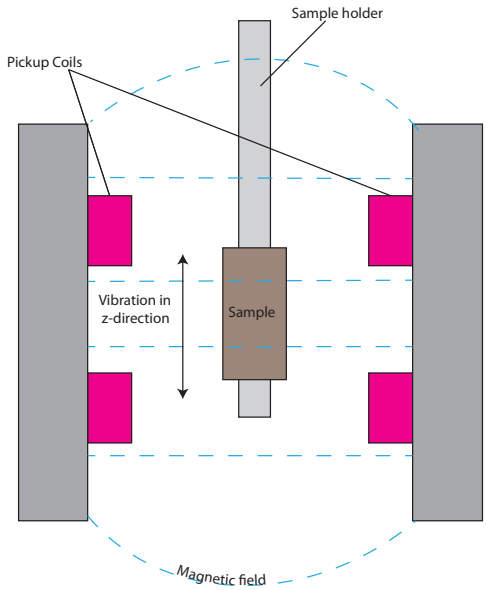

Figure 22: *Schematic of VSM setup. The sample is placed in the middle of a magnetic field and vibrated along the z-axis. The induced voltage in the pick-up coils are the out-put signal.*

For thin films the measurements will be from both film and substrate. In the case of a diamagnetic substrate, this contribution must be subtracted to find the magnetic moment of the film. From [67] the susceptibility of STO is found to be;

$$\chi_{dia}(STO) = -60 \times 10^{-6} emu/mol = -0.84 \times 10^{-3} memu/cm^3 \qquad (17)$$

where the conversion has been done based on that there is 5 atoms in a unit cell of volume $V = a^3$.

The VSM measurements in this work where done by Thomas Tybell, Mark Rzchowski and Chang-Beom Eom at Wisconsin University - Madison.

4 Results and Discussion

The aim of this work has been to achieve control at the atomic level of the growth and surface structure of (111) oriented thin films. To obtain control the parameters of growth must be studied and identified. The study consists of three parts; preparation of substrate surfaces, the growth mode of films and magnetic properties, where the emphasis lays on the growth mode.

In the growth mode chapter sections of consecutive control are presented. First, we look at the how the substrate surface affects film surfaces. Second the growth mode of the films is reviewed, for film thickness ranging from a few monolayers to 70nm thick films. The growth is monitored revealing a critical thickness where growth becomes three dimensional and unstable. The growth transition is tunable by growth parameters. In this work the dependence on temperature; i.e., the diffusion of ad-atoms is investigated. Third interface effects are studied, showing a possible band of strain at the interface and an additional two dimensional growth transition during the first monolayers. The last section speculate if step-edges could be a strain source, resulting in the surface breakup.

4.1 Substrate surface

This section concerns itself with control of the $SrTiO_3(111)$ surface. In the project step-and-terrace structure of the substrates were obtained [3]. In the current work, the control of substrate surfaces has been enhanced. The effect of the different preparation methods is compared, and a thorough review of the HF-etched samples are shown. Further the relation between crystallographic orientations and surface features is discussed, indicating surface energies and symmetry of the substrate.

4.1.1 Substrate preparation

All three methods of substrate preparation resulted in a step-and-terrace structure, as seen in the AFM images in figure 23, but step-heights and step-edge form where profoundly different.

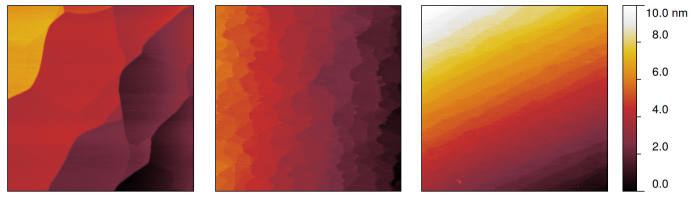

Figure 23: *AFM images of the three substrate preparation methods, all three images are $3\times3\mu m$, and 10nm height scale. Image a) show step-bunching, while both b) and c) results in 0,23nm steps. Image a) has meandering, b) faceted and c) straight terraces.*

Substrates prepared with the standard procedure and 40mL DI-water (an example is shown in figure 23 a) are inconsistent from batch to batch with different

degrees of step-bunching. The edge-contours are observed to be both meandering and faceted. In addition, there are discrepancies in step-height within individual substrates ranging from unit cell height of $0.23nm$ to several nanometers high.

Substrates etched with 80mL DI-water, figure 23b, on the other hand are all consistent with uniform step-heights of $0.23nm$ and step-widths of $150nm$. In this case the step-edges are faceted, not meandering.

Substrates etched with buffered HF (figure 23c) show consistent result for each substrate preparation, but the degree of step-bunching varies according to dipping time and annealing temperature. The variation of step-bunching for the HF-prepared samples is plotted in figure 24 a, where a map of step-height and step-widths for different annealing temperature and dipping times is shown. The colored areas show the distribution of step-heights and widths for each preparation method using HF as the etching chemical. In figure 24, samples annealed at $1200°C$ are plotted as triangles and the distribution illustrated with yellow areas. Samples annealed at $1150°C$ are plotted as squares and the distribution illustrated in green, while samples annealed at $1050°C$ are plotted as circles and the distribution illustrated in blue. In figure 24a it is clear that annealing times of $1200°C$ and $1150°C$ (specified in respectively yellow and green areas) show a variation of several decades of both heights and widths. Annealing time of $1050°C$ on the other hand has a variation of less than a decade.

The dipping times are illustrated by varying transparency, where the plotted symbols are light grey for low dipping times (15s), grey for 30s dipping time and black for 45s. The colored mapped areas are as well more transparent for lower dipping times. Generally low dipping times of 15s and 30s generally lead to a larger variation than the higher dipping time of 45s for all temperatures. It can be seen particularly for $1050°C$ annealing in figure 24 b. Light blue areas (15s dipping time) have step-heights from $0.2 - 0.5nm$ and widths from $0.2 - 0.6\mu m$. Medium blue areas (30s dipping time) have step-heights of only $0.2nm$, but step-widths of $0.2 - 1.2\mu m$. The dark blue area (45s) on the other hand is constricted to small area. Dipping time of 45s results in only $0.2 \pm 0.04nm$ high and $0.3 \pm 0.1\mu m$ broad steps. AFM image and height profile of the step-edges are depicted in figure 25. The uniform atomically defined straight step-and-terrace structure is found to be reproducible.

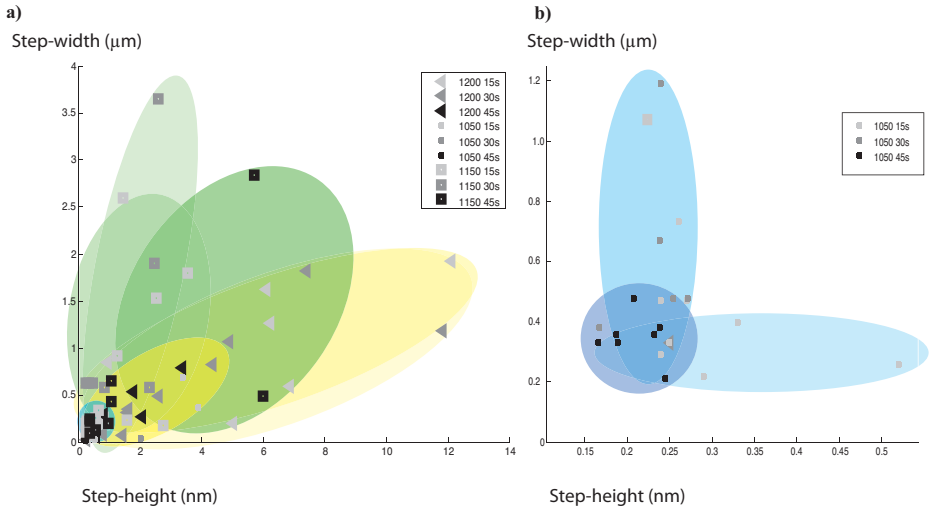

Figure 24: *HF-preparation: Variation of step-height and terrace-width for the different annealing temperatures and dipping times. Samples annealed a* $1200°C$ *are plotted as triangles and the distribution illustrated with yellow areas,* $1150°C$ *are plotted as squares and the distribution illustrated in green and samples annealed at* $1050°C$ *are plotted as circles and the distribution illustrated in blue. The plotted symbols are light grey for 15s, grey for 30s and black for 45s dipping times. The colored mapped areas are as well more transparent for lower dipping times. a) The distribution of step-heights and widths are profoundly less for* $1050°$ *than the other annealing times. b) The distribution of step-heights and widths are profoundly less for 45s dipping time than the other dipping times.*

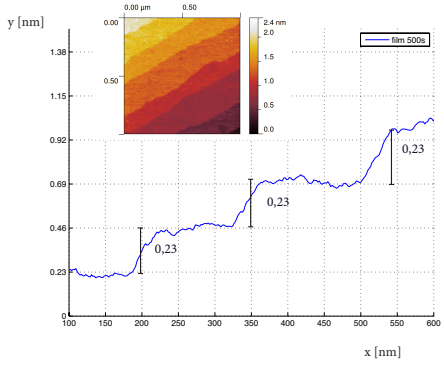

Figure 25: *AFM image and height profile of the best result from HF-etching showing steps of one unit cell height,* $0.23nm$*. The structure is reproducible for dipping time of 45s and annealing time of* $1050°$*.*

4.1.2 Crystallographic characterization of substrates

The substrates crystal structure where characterized by XRD, TEM and RHEED. The FWHM from the XRD where measured to be 0.010∘ for both DI-etched and HF-etched substrates. The lattice-parameters in all directions where found to be $0.3905nm$, confirming the cubic structure.

A detailed study of the RHEED pattern while rotating the substrates around the surface normal was done. In figure 26 the diffraction pattern is depicted with a normalized color scale according to azimuth angle. The diffraction pattern is half-circular and rotates around the central spot with the azimuth angle. Changes of 0.1° change the pattern, indicating high sensitivity.

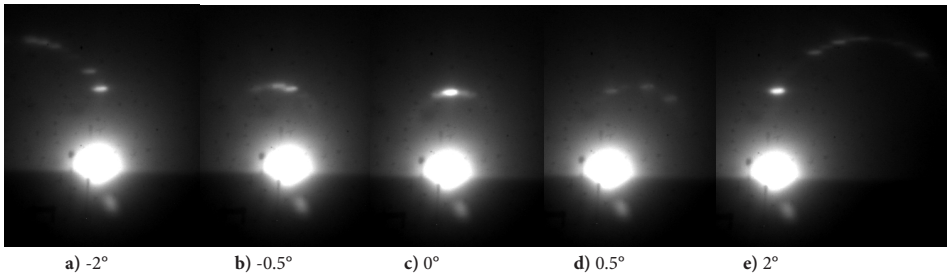

Figure 26: *RHEED patterns for different azimuth angles, showing high sensitivity in the diffraction pattern.*

The pattern repeats itself every 30°, and is shown in figure 27 From visual inspection the pattern is oriented towards the central spot at $30° * n$ from the substrate axis. The same pattern is apparent for all types of surface preparation.

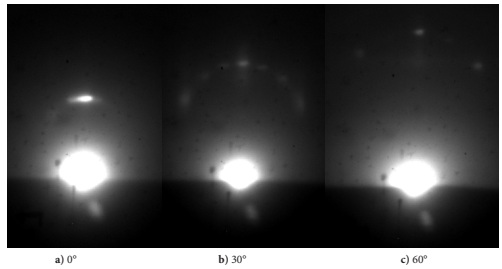

Figure 27: *RHEED patterns show a semicircle each* 30° *azimuth. The tilt of the sample has been held at the same value for all three images, accounting for the different distance from the main spot.*

In figure 28a the surface crystallographic axes are shown schematically. HF-etched substrates show straight step-edges at an angle of 30° from the substrate axis as illustrated in figure 28b. For faceted substrates the edge-contours cut off at angles of 60° and 120° with each other, 30° degrees with the axis of the substrates,

such that the terrace becomes parallel to the sample axis. The angles are illustrated in figure 28c. To determine if the step-edges are along certain crystallographic axis, TEM and XRD are used. TEM studies show that the substrate edge axis is $[\bar{1}0\bar{1}]$ and $[1\bar{1}2]$ (not shown). XRD alignment for $< 110 >$ measurements indicate that $30°$ from the substrate edge lies the $< 110 >$ family of directions.

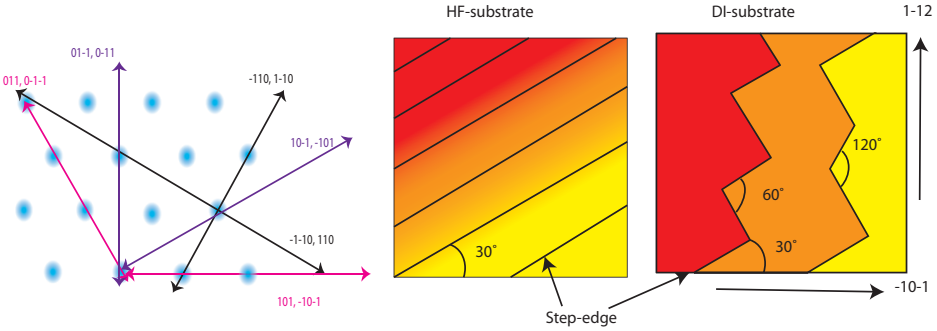

Figure 28: *Schematic of the step edges and crystallographic axis. a) the* $< 110 >, < 101 >, < 011 >$*-directions in the hexagonal surface, where black lines are parallel to the straight steps, while purple and pink lines are parallel to the faceted edges.b) HF-etched substrate with straight edges* $30°$ *from the substrate edge c) DI-etched substrate with faceted step-edges at* $60°$ *and* $120°$*.*

4.1.3 Discussion

The results from section 4.1.1 confirm that correct substrate preparation leads to the desired step-terrace surface structure of atomic well-defined straight terraces with step-heights of one unit cell. The height of the step-edges $(0, 23nm)$ indicate single termination as it accords with the lattice parameter in the (111) direction for STO and the experimental lattice parameter found from the XRD measurements. Which termination is not possible to tell from our measurements, but it is believed to be Ti^{4+} according to etching chemistry theories.

The optimization of the substrate preparation presents that small differences can give large effects on the surface structure. Increased annealing temperature leads to step-bunching, in accordance with earlier experiments, as well as limited amounts of etching reactant. Increased dipping times in HF on the other hand resulted in uniform step-heights, contrary to earlier findings [41].

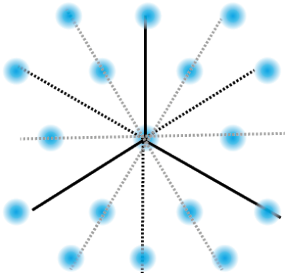

Figure 29: *The obtained symmetry from RHEED; the blue circles represent the atomic layer. Straight lines represent the 3-fold symmetry, dotted lines the show the same symmetry axis in the opposite direction and brown dotted lines show second order symmetries.*

The RHEED study of the diffraction pattern confirms a two-dimensional surface structure, indicated by circular diffraction patterns. The repeating of the pattern every 30° indicates a 12-fold symmetry, which is shown in figure 29. The honeycomb structure is clear with 3-fold symmetry (indicated by straight lines). However, RHEED cannot distinguish between equal symmetry operations, so the dotted lines in figure 29, must also be taken into account. In addition, RHEED will measure second order symmetries indicated by brown dotted lines in figure 29. The second order symmetries should have a different distance measured between the diffuse spots than first order symmetries, as the distance between atoms is different. In figure 27b and c such a difference is clear, while the comparison of figure 27a is not as easily achieved as the semi-circle lays much closer to the main spot. For figure 27b the distance between the diffuse spots is smallest, indicating that this is the $< 1\bar{1}2 >$ crystallographic direction, while figure 27c is the $< 110 >$ direction (the surface directions are shown in figure 28a). The RHEED signal confirms the hexagonal surface symmetry, and can be used to find the crystallographic directions as well.

The DI-water-etch show faceted step-edges of 60° and 120°, which accords with the expected hexagonal symmetry, and indicate that the surface energy for these

substrates is equal at all six directions of the crystal hexagon. The HF-etched substrates; on the other hand, show straight steps, always in the same direction indicating that one of the directions is preferred. XRD alignment indicates that the step-edges of the HF-etched substrates are oriented along one of the $< 110 >$-directions, while the faceted step-edges are along different $< 110 >, < 101 >, < 011 >$-directions. The different directions are shown in figure 29a, where black lines are parallel to the straight steps, while purple and pink lines are parallel to the faceted edges. The $\{110\}, \{101\}, \{011\}$-planes have less broken bonds than the $\{111\}$ planes, so that the surface energy is less at the $\{110\}, \{101\}, \{011\}$-planes. The preferred $< 110 >$-direction of the step-edges for HF-etched substrates may come from that the miscut is in a special direction, but this is not confirmed by the producer of the substrates.

4.2 Growth mode

In the previous project thin films of LSMO/STO(111) of step-and-terrace structure where obtained, but the growth was seen to be unstable, the surface breaking up at a certain thickness. In order to elucidate the mechanism behind this instability, in this work the growth mode has been investigated in more detail. Films have been grown at different thicknesses, ranging from a few monolayer to 70nm. This gives us a picture of how the growth develops with "time" as the films get thicker. The growth mode is categorized by dimensionality, surface structure and crystallinity.

4.2.1 In situ measurements

$In-situ$ measurements by RHEED are a powerful tool to monitor growth. In this work the RHEED diffraction patterns have been used decide dimensionality of the growth, and the intensity measurements to indicate roughness transitions in the growth.

To measure if the growth is three or two dimensional RHEED diffraction patterns have been taken before, during and after deposition. Generally (as already discussed in section 4.1) the substrates depict a semicircle of bright spots (figure 30a). During growth this picture alters to different patterns as seen in figure 30. Generally the spots become more drawn out and weaker than earlier. Three different scenarios have been observed. In figure 30b, the spots have changed position completely, into a quadratic pattern indicating 3D formations. In figure 30c, the spots are now aligned in a line, instead of a semicircle, also indicating 3D growth. Finally in figure 30d, the spots remain in place, only weaker and more blurry than before. The final scenario indicates a continued 2D surface. The change to the first scenario is rapid, happening at around 100s after beginning the deposition. The change to the second scenario is slower, beginning from 100-300s after deposition start. When the 2D diffraction pattern is obtained AFM images confirm the 2D structure, while when the different 3D patterns are obtained AFM images show both 2D structure, broken structures and 3D structures.

The RHEED-intensity data have been recorded for each deposition and generally show an intensity profile as in figure 31. The intensity drops as the laser starts, for around 100 laser pulses (100 seconds), then the intensity increases again and reaches its top at around 250-300s, before the intensity decreases slowly throughout the rest of the growth. This similar pattern is found for all growths, independent if the result is a two-dimensional structured step-and-terrace film or a three-dimensional unstructured film.

For growth of films on top of substrates of uniform straight atomically steps (HF-etch), some oscillations has been observed, as shown in figure 32. The purple intensity profiles (main specular spot) show an oscillation of two unit cells (30s), while the green intensity profile (right diffuse spot) show an oscillation of one unit cell (15s).

The RHEED data obtained do not give conclusive result of the dimensionality or mode of growth, but it is clear that there is a transition in growth at around 100s after deposition. This would be at 6-7 monolayers of growth.

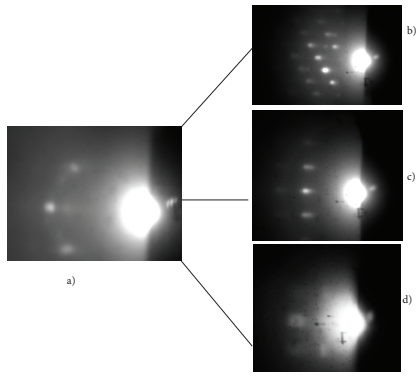

Figure 30: *RHEED diffraction patterns. a) Substrate diffraction pattern b) Quadratic diffraction pattern c) Linear diffraction pattern d) semi-circle diffraction pattern.*

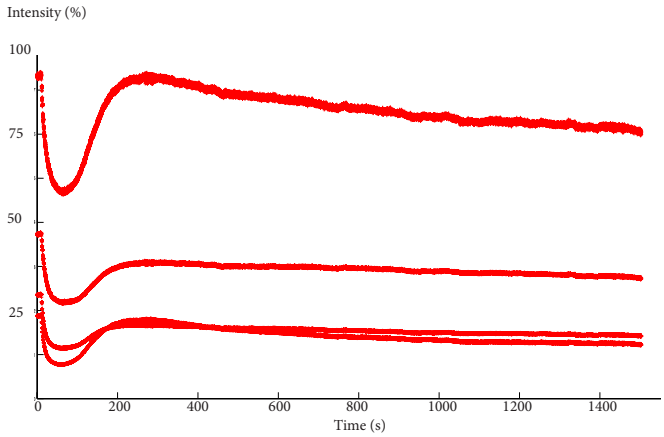

Figure 31: *Typical RHEED intensity profile. The profiles are from different spots in the diffraction pattern. The diffraction patterns show a transition from a semicircle to a quadratic pattern.*

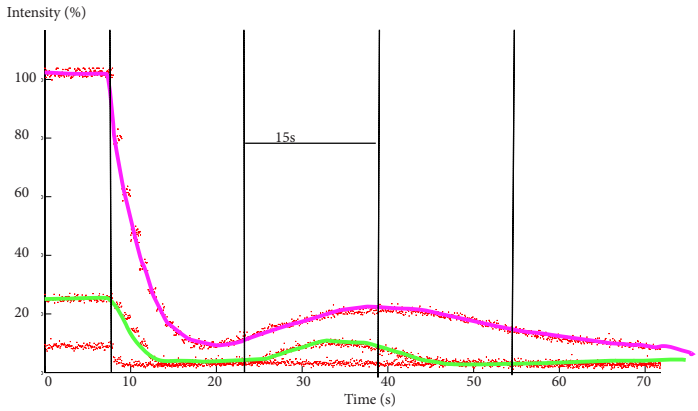

Figure 32: *RHEED intensity profile showing possible oscillations. The black dotted lines are placed 15s from each other, which is the expected time for one monolayer.*

4.2.2 Substrate influence on film growth

In the previous project, it was found that step-and-terrace structure on the substrate where essential to obtain step-and-terrace structure for the films. In this work the effect of different step-and-terrace structures on films has been investigated.

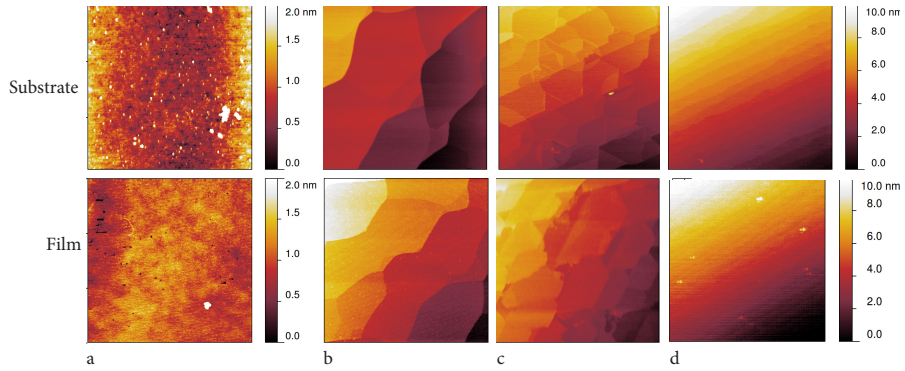

Figure 33: *The surface structure of the substrate decides how the surface structure of the film is; a) as-polished substrate and film, b) step bunched substrate and film c) faceted substrate and film and d) straight step-edge substrate and film. All images are* $3 \times 3\mu m$

.

The growth has been done under similar conditions, which have been proved by earlier research [3] as good growing conditions. All the films are grown for the same amount of time (500s), yielding the same thickness; 7nm. Figure 33 shows AFM images of substrates and corresponding films, all images are $3 \times 3\mu m$ in area. Figure 33a show an as-polished substrate without pretreatment before and after growth. The substrate is "flat" with no apparent structure or pattern on the surface, but for some contamination laying on top. The roughness (RMS) is measured to be $0.36 \pm 0.01nm$. The film is similarly flat with a roughness (RMS) of $0.20 \pm 0.03nm$. In figure 33b a step-bunched substrate is shown with its corresponding film. Also in this case the film topography resembles strongly the substrate topography. In both cases, the height of the steps varies between $1 - 2nm$ and terrace widths between $0.5 - 1\mu m$. The step-edges are meandering in form, swinging $60°$ back and forth in a winding curve. In figure 33c a substrate of atomic plane steps and faceted edges of $60°/120°$, are shown along with its film. The steps of the film are exactly as in the substrate, with heights of $0.23nm$ and terrace widths of $500nm$. The faceting is also reproduced, but the step edges of the film are less straight and more unordered. Finally, figure 33d depicts a substrate with straight uniform steps, which are also reproduced in the film. The step-heights of both substrate and film are $0.23nm$, the terrace widths $150nm$. Also in this case the film steps are a bit less abrupt than the film, but the structure is repeated.

4.2.3 Temperature

As discussed in section 2.3, diffusion across the surface a determining factor for the growth. To elucidate the diffusion mechanism during growth in this work a temperature study has been performed.

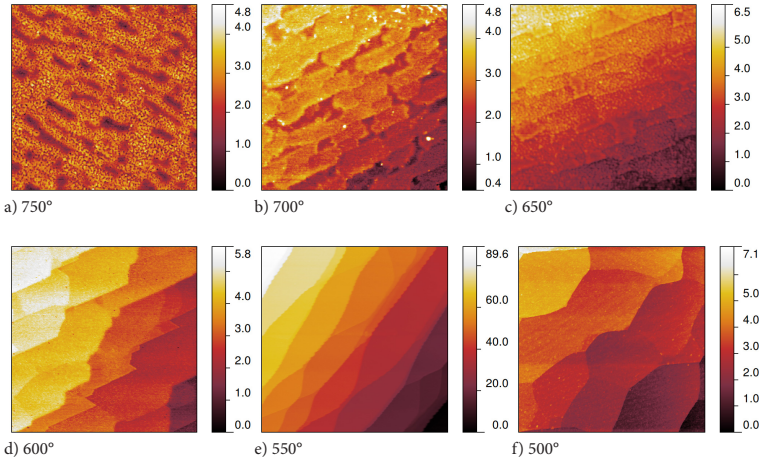

Figure 34: *AFM images of 7nm films grown at different deposition temperatures a) $750°C$, b) $700°C$, c) $650°C$, d) $600°C$, e) $550°C$ and f) $500°C$. All images are $3 \times 3\mu m$, and the height scale are depicted for each image.*

AFM images of films of 7nm grown at growth temperatures between $750-500°C$ are shown in figure 34, all images are $3 \times 3\mu m$. The substrates used where prepared by 40 ml DI-etch, with different degrees of step bunching, with step-heights between $0.5-10nm$. An apparent feature is the evolution of surface structure; from rough to step-and-terrace with decreasing temperature. At $750°C$ (figure 34 a) it is hard to see the step-and-terrace structure, with both large cracks and small holes between $0.6-2nm$ deep. But the surface is not unordered, the cracks are somewhat aligned. Decreasing the temperature to $700°C$ (figure 34b) results in a more ordered film, with terraces clearly in the topography. But at the step-edges, similar cracks as the $750°C$ film are found. The step-terrace structure seems to break at the step-edges for this temperature. The break is measured to be $2nm$ deep. The measured depth of the holes is the minimum depth, limited by the AFM-tip form. A further decrease to $650°C$ is shown in figure 34c. Here, the step-edges are defined, with no break-up structure, while the terraces on the other hand seem to be rougher. The films grown at $600°C$, $550°C$ and $500°C$ all show clear step-and-terrace structure, with well-defined edges and smooth terraces with an RMS roughness of $0.06 - 0.08nm$.

It is clear that increased temperature mediates a surface breakup of the surface, while decreased temperature results in smooth step-and-terrace structures. This is in accordance with theoretical predictions for strained surfaces (sec. 2.1.2), where decreased diffusion suppresses second-layer-nucleation.

4.2.4 Critical thickness

The surface break-up in the previous section and earlier work, indicates that the growth is unstable after a certain critical thickness. To determine the manner of this instability a thickness-study for different temperatures was performed.

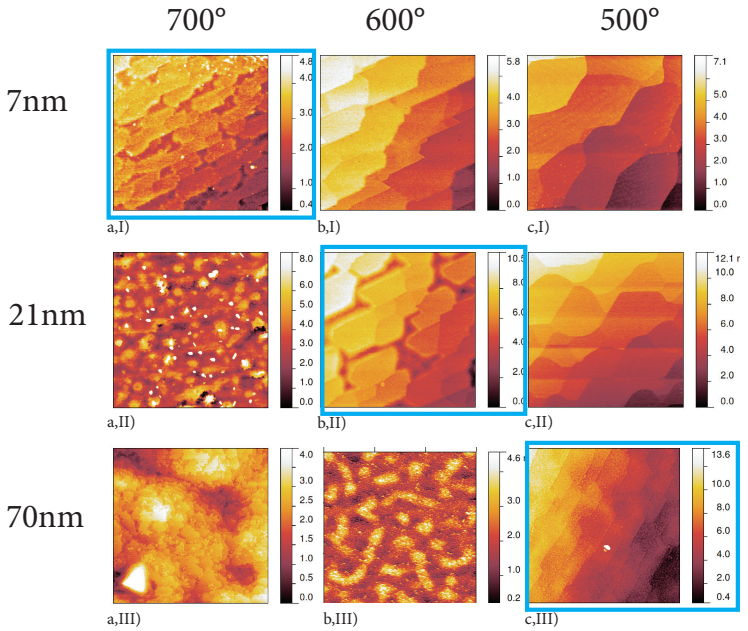

Figure 35: *AFM images of films of different temperatures and thickness. a)* $700°C$*;, I) 7nm II) 21nm III) 70nm, b)* $600°C$*; I) 7nm II) 21nm III) 70nm, c)* $500°C$*; I) 7nm II) 21nm III) 70nm. All images are* $3 \times 3\mu m$*, and the height scale are depicted for each image. Blue squares represent images where growth transitions are observed.*

Films with thicknesses between $7nm - 70nm$ have been grown for three different temperatures; $700°C$, $600°C$ and $500°C$. The substrates were prepared by 40 ml DI-etch, with different degrees of step bunching; step-heights are between $0.23 - 3nm$. The films step-heights and step-edge form are consistent with the substrates (not shown). AFM images of the samples at $7nm$, $21nm$ and $70nm$ are shown in figure 35.

For $700°C, 7nm$ (figure 35a,I) the surface is broken with a crack-like structure between terraces. At $21nm$ (figure 35a,II) the surface is full of small islands and cracks of different height, while the $70nm$ (figure 35a,III) thick film show larger 3D islands. The islands have a "wedding cake" or pyramidal form, each layer becoming smaller than the one underneath. One island consists of around 10-12 layers. A close-up show that for the $21nm$ (figure 35a,III) the islands are in this "wedding cake" form as well, with around 3-4 layers per island. The step-heights of the layers are around $0.4 - 0.6$ for both samples. A $4nm$ sample where also grown at $700°C$ (not shown) which yielded a smooth step-and-terrace structure.

For $600°C$ at $7nm$ (figure 35b,I) the surface is clearly step-and-terrace, with no indication of 3D growth. At $21nm$, (figure 35b,II) the same broken, crack-like surface as in figure 35a,I is seen, the cracks following the step-edges. At $70nm$ (figure 35b,III) no step-and-terrace or pyramidal forms is observed, but rather "fingers" of oval forms. The form are similar to the crack-like surface, but with 3D growth on top of both terrace and crack, as well as the $750°C$ in figure 34a.

The $500°C$ samples show step-and-terrace structures for all thicknesses, but the $70nm$ (figure 35c,III) have rather rough terraces compared to the others. Other samples grown at $500°$, $70nm$ show more broken-up surfaces and signs of 3D growth, indicating that this thickness is at a transition point.

The critical thickness is observed for all temperatures, indicating that the growth is unstable. However decreased temperature delays the critical thickness till at least 70nm thick samples.

4.2.5 HF- substrates critical thickness

To determine the effect of substrate surface on the critical thickness, a second thickness series was deposited on substrates of HF-etched substrates with atomically defined step-edges.

The series where done at 500°, the AFM images are shown in figure 36. At $7nm$ (figure 36a) the step-and-terrace structure is clear, but on top triangles are seen. At $21nm$ (figure 36b) there is a clear step-and-terrace structure, while at $70nm$ (figure 36c) the surface structure show 3D growth and particles, not the broken structure expected from the DI-substrates.

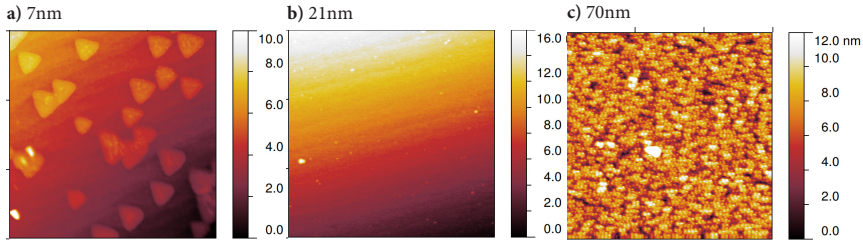

Figure 36: *AFM images of films deposited on atomically defined step-and-terrace structure substrates. a) 7nm thick film, b) 21nm thick film c) 70nm thick film*

Initially, the step-and-terrace structure seems to follow the substrate completely for the first regime of the growth, but a closer look at the step heights shows some variations. Height profiles from the AFM images are used to get precise measurements of the topography, as seen in figure 37. For the substrate all step edges are measured to be $0.23nm$, while the films show step heights of 0.34 and $0.46nm$ as well. Observations of several films show that the thicker films have an increased density of $0.46nm$-edges, compared to thinner films. At the left side of figure 37 AFM images of substrate, $14nm$ film and $21nm$ film are shown. All images are $3 \times 3\mu m$, but the color scale changes from 10nm to 16nm, indicating an increase in density or step-height. The step-widths of the substrates are not as uniform as the height, having widths between $100 - 200nm$. This is the case as well with the films, and no general trend of decrease or increase can be measured. In general the films are not as smooth as the substrates, as seen in figure 37. The RMS has been measured at the terraces yielding respectively, $0.06nm$, $0.1nm$ and $0.2nm$ for substrate, $14nm$ film and $21nm$ film.

The HF-etched substrates yield the same growth mode as the DI-etched substrates in the previous section (section 4.2.4), but the 3D growth is observed at an earlier point than for DI-substrates. It is also observed that step-bunching is a part of the two dimensional growth before the critical thickness.

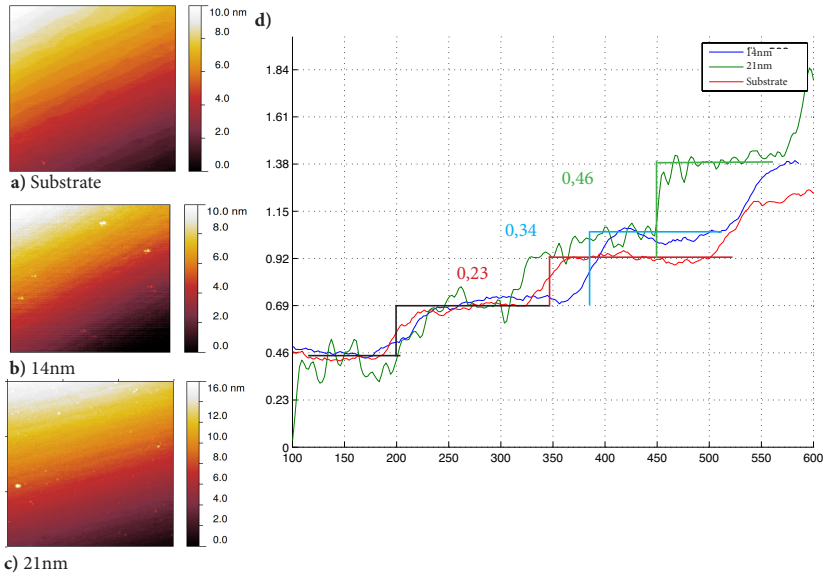

Figure 37: *The evolution of step-edges with thickness. AFM images of a) substrate, b) 14nm thick film and c) 21nm thick film. All images are* $3 \times 3\mu m$*, and the height scale are depicted for each image. d) profiles taken from the images show a tendency of step bunching with increased thickness. Red line are from the substrate, blue from 14nm thick film and green from 21nm thick film.*

4.2.6 Crystal structure

To confirm epitaxial growth and determine the crystal structure XRD and TEM where used.

In figure 38, a typical $\theta - 2\theta$ scan is shown of the (111) peak. The substrate peak is found to have an c-lattice parameter of 3.905Å in the pseudo cubic notation, which is the tabulated number. The film peak is shifted slightly, indicating a compression of the c-lattice parameter. Averaging over all measurements d_{111} is found to be $d_{111} = 2.2234 \pm 0.003$Å compared to $d_{111} = 2.34$ Å for unstrained LSMO. In the pseudo cubic notation, the c-lattice parameter is measured to be $c_{LSMO} = 3.851 \pm 0.003$Å.

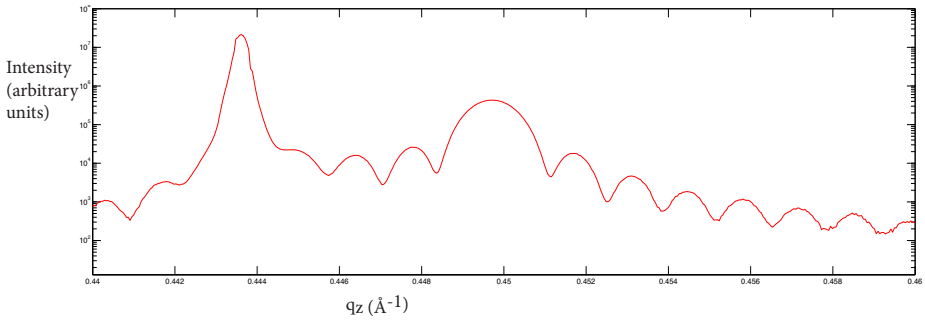

Figure 38: *Typical $\theta - 2\theta$ scan of the (111) peak with logarithmic scale of the intensity. The scale show the reciprocal lattice parameter q_z for the (222) peak.*

XRD rocking curves have also been measured to insure the crystallinity of the films. The average full-width-half-maximum (FWHM) for substrates has been found to be 0.010° for substrates and 0.025° for films, which confirm coherent growth. A reciprocal space map of the (033) peak, aligned by the (112) direction in h-direction is shown in figure 39. The in-plane lattice parameter is found to be in total alignment with the substrate, again confirming the coherent growth. The out-of-plane parameter is found to be $d_{111} = 2.2235$Å, as with the $\theta - 2\theta$ scan.

The symmetry of the films has been found by ϕ-scan, shown in figure 40a. A threefold symmetry is found, confirming the hexagonal symmetry. No indications of domains where observed. In figure 40b and c, TEM diffraction patterns from plane view and cross section respectively are shown. The hexagonal symmetry is unambiguous, a further indication that the the film is in the (111) direction, and possibly mono crystalline.

The thickness of the films has been determined by approximations of the thickness fringes in the $\theta - 2\theta$ scans. In figure 41 two samples grown at 500°, with confirmed 2D surfaces by AFM at different thickness is shown. It should be noted that the lattice parameters are the same for the two samples, confirming that the growth does not relax with thickness. The $5000s$ sample is found to be $76nm$ and the $3000s$ is found to be $41nm$.

Judging from the time of deposition and the obtained thicknesses, an average

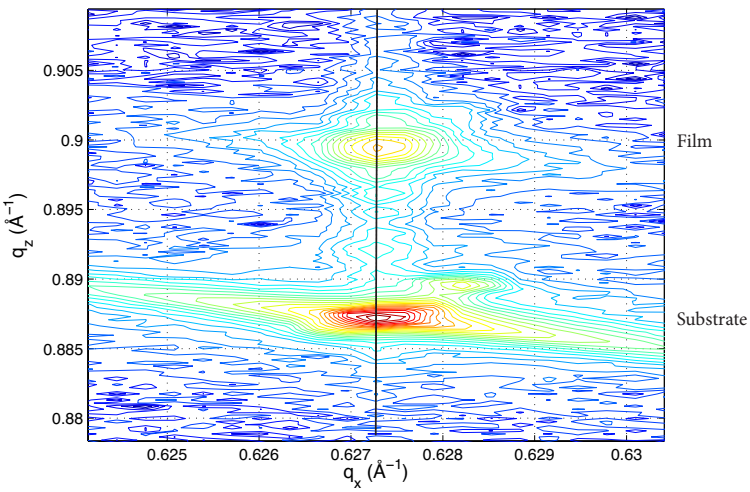

Figure 39: *Reciprocal space map of the 033 substrate peak as a function of q_x and q_z. The dotted line show how q_x is the same for substrate and film. Note that the reciprocal lattice parameter for substrate and film in q_z is double of the $\theta - 2\theta$scan in figure 38 as the reciprocal space map is aligned for the (112) peak.*

deposition rate of $15.4s \pm 0.8s$ per unit cell is obtained. This is the number used to convert between time and thickness throughout this work.

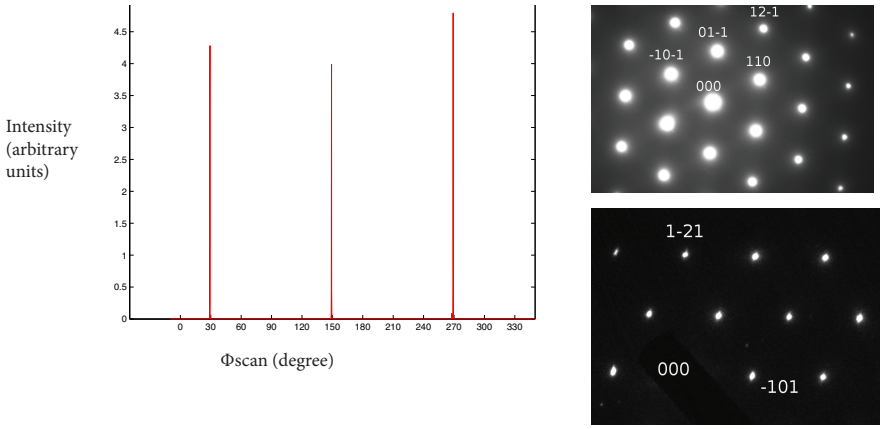

Figure 40: *Symmetry: a) ϕ-scan of the 303 peak of LSMO film, depicting a six-fold symmetry. b) TEM diffraction pattern plane view depicting a hexagonal symmetry.c) TEM diffraction pattern cross section depicting a hexagonal symmetry.*

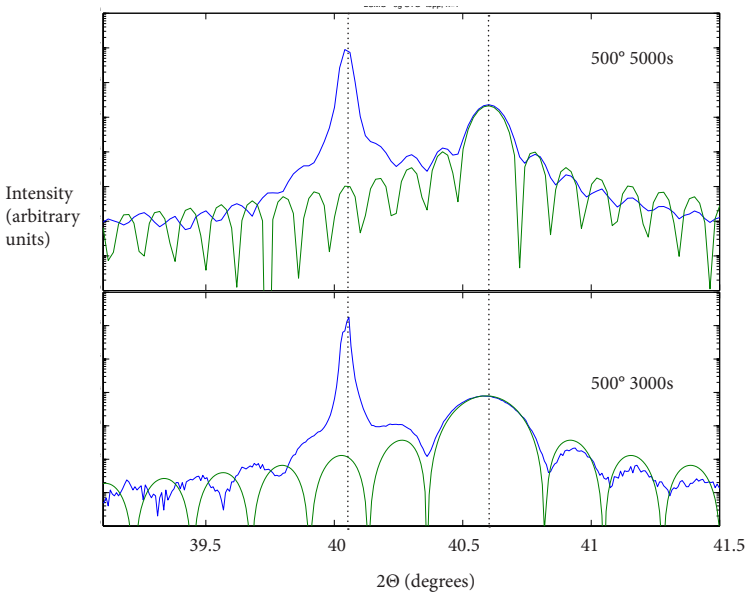

Figure 41: *2θ-θ scans with approximations for the thickness fringes, for two different thicknesses. Both samples have the same lattice parameters as shown by the dotted lines.*

4.2.7 Interface strain

The instability in growth are due to the strain in the film. To determine the strained state of the films, TEM images of different resolution have been taken of the films.

In figure 42 two cross sectional TEM images of the interface are shown, both taken at (111) zone axis, but at different resolution. The HRTEM cross-section image in figure 42a confirms the crystallinity of both substrate and film, with well-defined atomic planes. Exactly at the interface a band of contrast is seen, attributed to a larger strain in this area. In the cross section image in 42b the same interface band of strain is seen. This strained layer is measured to be around four monolayers. The strained layer is seen for films of both DI-etched and HF-etched substrates and at different resolutions, such that substrate preparation or TEM preparation does not seem to be an explanation. In figure 42c diagonals are seen coming from the interface growing through the film. These diagonals can be both elastic domains and strain, the correct answer is not confirmed yet. The distance between them is measured to be $150nm$. Preliminary measurements show that the diagonals form approximately $15°$ with the interface, which is the $< 121 >$family of planes.

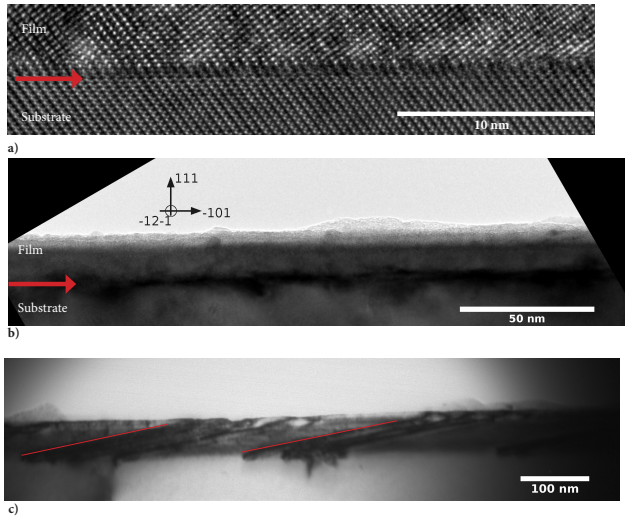

Figure 42: *TEM cross-sectional images of the interface. The interface band is indicated by the red arrow. a) High resolution TEM showing contrast at the interface b) Cross-sectional TEM confirming the contrast seen at the interface c) Possible dislocations or elastic domains in the film shown by red lines.*

The possible strain band at the interface may be the responsible for the unstable growth, as strain accumulates with further film growth.

4.2.8 Interface growth

As already noted in section 4.2.1, RHEED intensities indicate that there is a second growth transition at around 100s after deposition. The possible strain interface band also indicates that something is happening at the first monolayers. To investigate the initial growth, a thickness series of films of the first monolayers where done, i.e. much thinner films than earlier where investigated.

Films of 2, 4, 9 and 17 monolayers (ML) where grown, AFM images are shown in figure 43. This corresponds to thicknesses of $0.46nm$, $0.92nm$, $2nm$ and $4nm$ respectively. The substrates used where DI-etched with atomically defined step-edges, and faceted step-contours. The growth was done at $500°C$.

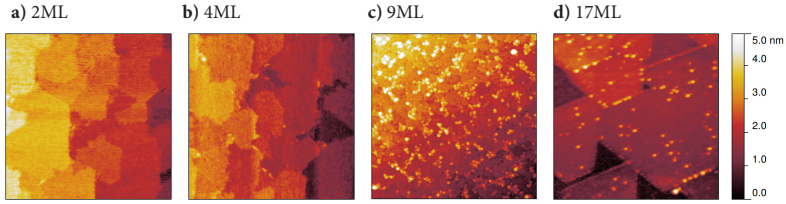

Figure 43: *AFM images of films of a)2 monolayers thick, b) 4 monolayers thick, c) 10 monolayers thick and d) 20 monolayers thick. All images are* $1 \times 1\mu m$*, with the same height scale shown at the right side.*

At 2ML (figure 43a) the film looks exactly like the substrates, with step-heights of $1nm$, step-withs of $200nm$ and the faceted step-and-terrace structure. At 4ML (figure 43b) the film is almost the same, but it looks a bit rougher, though step-heights and withs are the same. At $9ML$ (figure 43c) the step-and-terrace structure is almost disappeared, and small clusters of particles are seen to dominate the surface. There seems to be a small tendency for the clusters to nucleate at the step-edges, but it is difficult to conclude as the steps are faceted. The height of the particles is around $0.5nm$, which is 2ML and indicates second nucleation. Then at 17ML (figure 43b) terraces show up again, but in a triangular form, with gaps between them and clusters at the step-edges. The clusters are also in this case found to be around $0.5nm$ in height, while the gaps are around $1nm$.

The RMS roughness of the samples grown at $500°C$ is shown in figure 44. To avoid substrate effects, the RMS roughness of the films has been divided by the RMS roughness of the according substrate. All RMS roughness measurements have been obtained from $1 \times 1\mu m$ AFM images. The substrate and 2ML film are equal, indicating at this point the growth follows the substrate completely. Then at 4ML the the roughness increases and at 9ML a maximum is found, indicating a roughness transition at this point, before the the roughness decreases again at 17ML (4nm). Including the thicker films grown at 500°, show that the RMS roughness keeps almost constant and low for further growth, before increasing largely at $70nm$ for the onset of 3D growth.

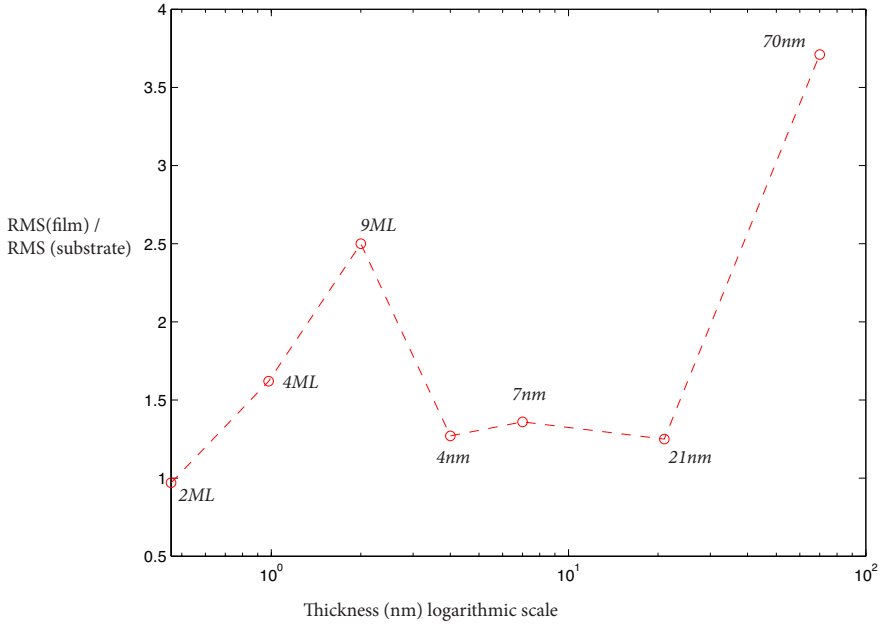

Figure 44: *The RMS roughness of films divided by the RMS roughness of the substrate as a function of thickness. All roughness measurements are done at* $1 \times 1\mu m$ *AFM images. The films were grown at* $500°C$*. The thickness is shown on a logarithmic scale to enhance visibility.*

A roughness transition is observed for the initial growth. The growth roughens after only 2ML, clusters forming triangles on top of the terraces, before smoothening to step-and-terrace structure again.

4.2.9 Step bunching

The surface breakup at the critical thickness was observed to be at the step-edges in the step-and-terraces structure. To further investigate the role of step-edges two series of films have been grown at equal parameters, with substrates of different degree of step bunching. The growth parameters were chosen to be at the critical thickness for the non-step bunched substrates, earlier defined as the blue squares in figure 35; $700°, 7nm$, $600°, 21nm$ and $500°, 70nm$.

The substrates where 1) non-step bunched DI-etched substrates with step-heights between $0.2 - 0.6nm$ and widths of $0.2\mu m$ and 2) step-bunched HF-etched substrates with step-heights of $2 - 5nm$ and $1 - 3\mu m$ for the $500°C, 70nm$. AFM images of the films are shown in figure 45, where all images are $3 \times 3\mu m$, except figure 45c. The $500°C, 70nm$ with step-bunched substrate is $10\mu m$ because of a larger factor of step-bunch than the others.

In figure 45 the non-step bunched films all show the broken-up structure at the critical thickness. Furthermore, it is clear for all cases that the step-bunched substrates result in step-and-terrace structures with clear edges and smooth terraces. For the $500°C, 70nm$ step bunched substrate, islands on top of the terraces are seen, reaching heights of $1nm$.

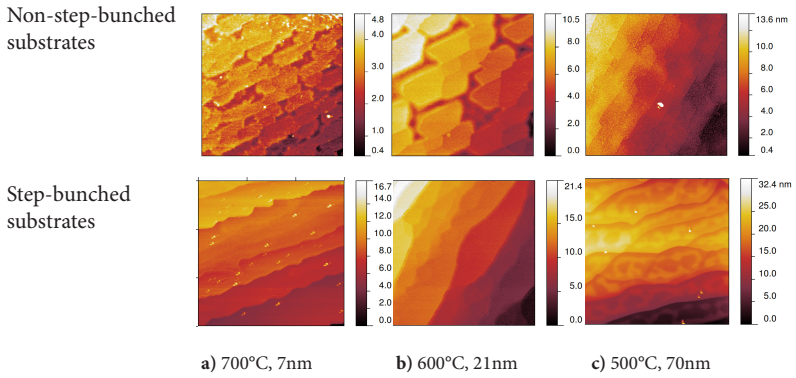

Figure 45: *Non-step-bunched substrates result in broken up structures, while step-bunched substrates result in step-and-terrace structure for the same growth parameters. a)* $700°, 7nm$*, b)* $600°, 21nm$ *and c)* $500°, 70nm$

Step-bunched substrates are observed to stabilize growth, delaying the critical thickness.

4.2.10 Discussion

Substrate influence It is clear that the substrate topography highly determines the surface topography of the grown films. As seen in the examples of figure 33, all features of the substrate surface structure are reproduced in the film. For unordered substrates unordered films are obtained, while structured substrates impose directionality and alignment on the film, with equal step-heights and widths. This indicates a large interaction between film and substrate, where the substrate constrains the film growth to its own features. It is also indicative of 2D layer-by-layer or step flow growth, as 3D/island growth would alter the surface topography.

The consistent dependence on substrate preparation gives an extensive control of the surface morphology of the films. Using the preparation parameters it is possible to tune the surface structure, controlling degree of step bunching and the directional alignment of the steps, into the desired product.

Temperature dependence Clearly decreasing the temperature optimizes the growth conditions for 2D growth. At high temperatures the ad-atoms diffuse from the step edges, making cracks as discussed in section 2.1.2. The depth of the cracks is about $2nm$(10monolayers) which indicates that it is not a result of non-full coverage, but a result of 3D growth. For strained films, a decrease in growth temperature is beneficial for several reasons. Primarily the substrate - film interaction increases, delaying the critical thickness of a film. Secondly, the diffusion length decreases, enabling dominance of coalescence of islands instead of second-layer nucleation. The gaps between islands are situated at the maximum of the local strain, where nucleation is unfavorable. If the diffusion length is too long, ad-atoms diffuse past these points, nucleating at the islands instead, such that gaps will rapidly grow into larger cracks. However, a short diffusion length will lead the ad-atoms to the gaps and fill them, as long as interlayer growth is still dominant. For $750°C, 7nm$ in figure 34 a the growth seems to be exactly at the critical thickness, where cracks have form between islands and island growth is dominant. For lower temperatures the 2D growth is stable, while higher temperatures result in unordered 3D surfaces.

Using the same growth parameters as in this study, optimal growth parameters of LSMO(001) have been found to be $700°C$, by our research group. The increased stability of LSMO(001) could be due to larger substrate-film interaction and less strain. A difference in substrate-film interaction is expected as STO(111) has a polar surface which might reconstruct prior to deposition, whilst STO(001) is neutral. Surface reconstructions may lead to larger strain in the film material, increasing the instability of the film.

Crystallinity The films are confirmed to be mono crystalline, of hexagonal symmetry and grown epitaxially on the substrate. The in-plane lattice parameters confirm a film of tensile stress, and the out-of-plane lattice parameter confirms a compression of the unit cell.

Growth mode from interface to the critical thickness From all the experiments the proposed growth mode is shown schematically in figure 46. At the

interface, the first few monolayers are exactly as the substrate. No islands or clusters are observed indicating 2D step-flow growth. The later formation of clusters, triangles and later step-and-terrace structure again, indicate that the growth mode goes through a roughening transition. The clusters grow in a triangular form. The triangular form is similar to the faceting found for the substrates. This indicates that also in growth, some crystallographic directions are more beneficial than others in the hexagonal symmetry. It is believed that the step-edges of triangles are along the $< 110 >, < 101 >< 011 >$ directions, as these directions have a lower surface energy than the (111) surface. The height scale for all images in figure **??** is equal, indicating that the surface has not changed profoundly, but rather changes between different types of 2D growth. As later growth has been confirmed to be layer-by-layer, it is prominent to believe a step-flow to layer-by-layer transition is seen for the first 20 ML.

The roughening stage around 9ML (135s) is confirmed by RHEED intensities, which decreases till 100s (7ML). Then, the RHEED intensities increase again, marking the transition to smooth 2D layers and layer-by-layer growth. The RMS roughness data (figure 44 show the same transition, with increasing roughness with thickness before a peak at 9ML, and decrease again as the growth starts to be layer-by-layer.

The possible interface strain band extends in the same length scale (4ML), to where the roughening transition starts. It is therefor naturally to believe that the growth transition and strain band are coupled. Lepetit et al [48] show that for LSMO/STO(001) the first 4ML are elongated instead of contracted because of the electronic interaction over the interface. A similar effect could be the reason for the strain band and growth transition as well. Because of the thin films involved this we were not able to confirm this by XRD.

The further growth show an almost constant RMS roughness until a sharp increase at thick films, indicating the second growth transition and the critical thickness. Looking at the diagonals of figure 35 (upper-left to down-right) the surface structure is similar for all temperatures. The growth evolution is similar for all temperatures, with only a delay for each temperature jump. The growth starts with 2D growth which evolves into 3D island growth at a critical thickness (indicated by blue squares in figure 35). The 2D-3D transition starts with a roughening, and breaks up at the step edges, which form cracks that rapidly deepens. The further growth is 3D and forms islands from the terraces, and valleys of the cracks. The critical thickness is different for different temperatures, confirming that lower temperature stabilizes the 2D growth and delays the critical thickness. The evolution of growth correlates well with theories and earlier research; the adatoms form islands which coalesce into smooth 2D films before a critical thickness when it becomes more favorable to nucleate the next layers before coalescence of the islands.

The HF-samples showed that while the step-and-terrace structure was still conserved, the surface experiences step-bunching and roughening. The roughening of the films may indicate preferential resputtering or an early transition to 3D growth. The increased roughness makes it harder to obtain exact step-heights, as

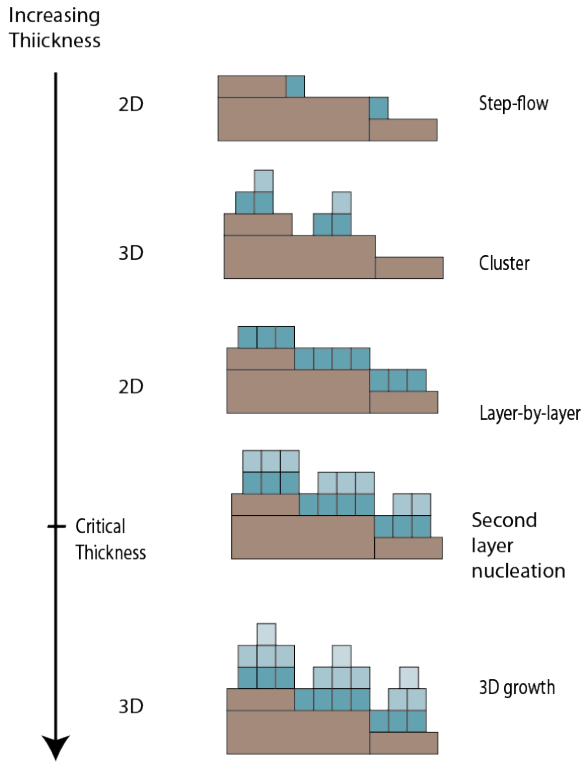

Figure 46: *The growth mode goes through several transitions; step-flow to layer-by-layer to 3D growth.*

the terrace itself is not as smooth. The observation of half-monolayer steps could therefore be an effect of the roughness of the terrace, instead of mixed-termination. The step-bunching could be a stabilization effect of the growth.

The effect of step-edges The transition from 2D to 3D growth is characterized by a break up of the surface structure at the step-edges. The breakup are explained by a tendency for second-layer- nucleation instead of filling of gaps between islands. The gaps between islands are situated at the maximum of the local strain. As break-up is seen at the step-edges, which indicate that the maxima of local strain are situated at the step-edges. In figure 47 some scenarios for step-induced strain is represented. For films with an out-of-plane lattice parameter different from the substrate, it is seen that step-edges will induce a certain shift in the stacking. To compensate for this shift dislocation may appear, as reported in an article from [50]. For mixed terminations anti-phase boundaries arise, resulting in stacking faults. For LSMO the out-of-plane lattice parameter is almost equal, but the unit cell is a bit tilted as seen in figure 47c. In this case the step-edge may induce dislocations to compensate for the tilt.

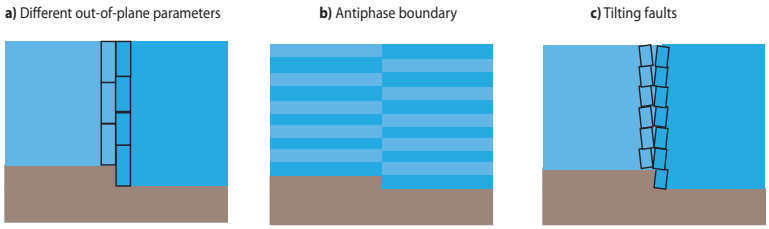

Figure 47: *Possible strain induced by step-edges; a) stacking faults to align layers from different sides of the step b) anti phase boundaries for mixed terminations, where the different blue colors represent terminations c) reconstructions because of tilting of the unit cell.*

In cross sectional TEM images (figure 42c) diagonals are seen coming from the interface growing through the film. These diagonals can be both elastic domains and strain, which of is not confirmed yet. Still, the distance between them ($150nm$), points to an origin of the step-edges. If the diagonals are dislocations, it would seem they start at the step-edge and grow in the forward direction at a certain crystallographic plane. Preliminary measurements show that the diagonals form approximately $15°$ with the interface, which is the $< 121 >$family of planes.

The step-bunched substrates are seen to stabilizes growth, delaying the critical thickness where breakup occurs. The critical thickness is determined by the substrate-film interaction, indicating that step-bunching leads to interaction over a longer distance. If the strain is localized around the step-edges, a step-bunching will lead to larger distances between local strain points. It is therefore, possible that the growth is stabilized as strain density points are lower. Another possibility is that such high steps are not as spatially abrupt as normal step-edges, making a crystallographic facet which are stable for growth. Thinking of the three possibilities sketched in figure 47, a step-bunched step could stabilize the difference in out-of-plane lattice parameter as the relaxation could be distributed over several unit cells. It could as well stabilize tilting, if the step is not as abrupt as a normal step edge.

4.3 Magnetic properties

The control of growth are a step toward control of properties for the interface. Though these are only preliminary results and require confirmation, the saturated magnetic moment of one of the films has been measured at room temperature to be $330 emu/cc$, which is higher than earlier reports.

4.3.1 Magnetic analysis

The measurements where done to a $500°, 70nm$ film with smooth surface structure, confirmed by AFM. The extracted data are shown below, where the diamagnetic contribution from the substrate is subtracted. The diamagnetism from substrate was calculated to be $0,84 emu/cm^3$. In figure 48 a typical hysteresis curve for in-plane and out-of-plane is shown. In figure 49 the anisotropy has been plotted in-plane as a function of magnetism and coercive field. The magnetism is almost constant at $250 emu/cc$ (1,5 bohr magneton per Mn), the coercive field drops from 4700 to $4200 A/m$. Out of plane measurements show a large component also at perpendicular field; 13° difference from the expected result.

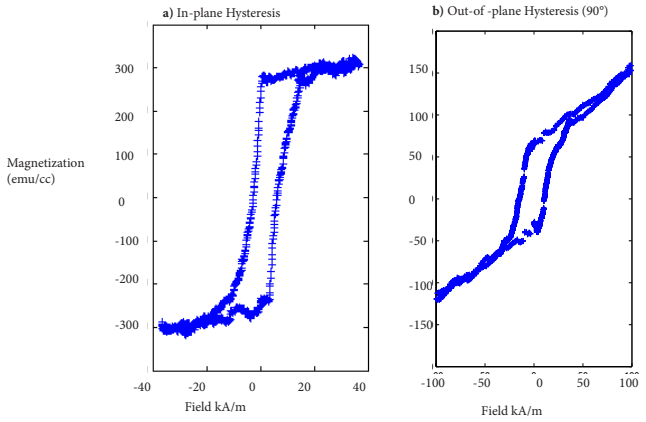

Figure 48: *Typical hysteresis curves for a) in-plane measurements b) out-of-plane measurements*

4.3.2 Discussion

The 3-fold symmetry of the crystal is expected to make magnetic domains which are 6-fold, as the measurements cannot distinguish equal symmetry operations (see figure 29). An anisotropy is therefor expected each 30°. In our measurements

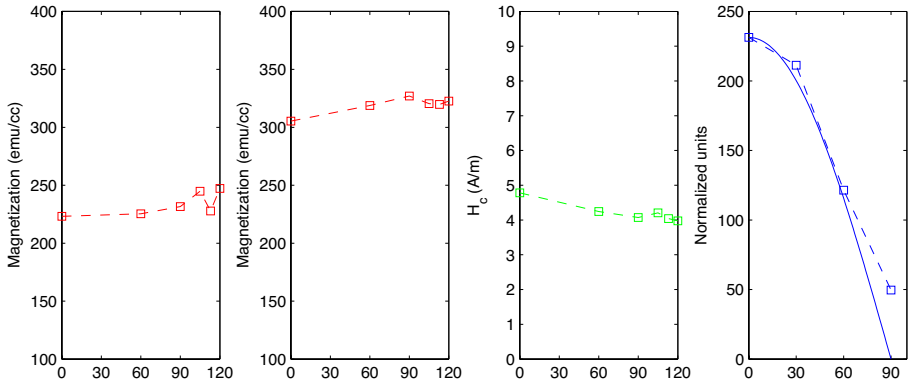

Figure 49: *Anisotropy measurements, where in-plane measurements are parallel to the* $< 110 >$ *direction at* $0°$*,* $60°$ *and* $120°$*. Out-of-plane measurements are performed from in-plane* $(0°)$ *to parallel to the surface parallel* $(90°)$*. a) In-plane anisotropy remnant magnetism b) In-plane anisotropy saturation magnetism c) In plane anisotropy coercive field d) out of plane magnetic components, dashed line is measured, straight line is the theoretical curve.*

for room temperature, no such anisotropy is found. The out-of-plane measurements are expected to go as the straight line in figure 29c, such that there are no out-of-plane components. As can be seen the measured moment is not 0 perpendicular to the surface. A small discrepancy could be due to inaccurate orientation of the sample since the orientation was done manually. However, in this case the measurements most be $13°$ wrong to get the expected result, which is unlikely. The large discrepancy therefor indicates that we have some out-of-plane contributions. The saturation magnetic moment is larger than previously reported for LSMO/STO(111), being $330 emu/cc$ for the saturation magnetism and $240 emu/cc$ for the remnant magnetization.

5 Conclusion and Further work

The aim of this work was to investigate how control of surface morphology and growth, in order to control properties, can be achieved for (111) oriented films of LSMO. Epitaxial single crystal films where grown by PLD, the structural characterization done by XRD and TEM. The surface morphology and growth where characterized by AFM and RHEED, while magnetic measurements where done at room temperature by VSM.

The control mechanism for surface morphology was found to be control of the substrate surfaces. The use of different preparation methods and parameters enabled tunable degrees of step-heights and favorable step-edge directions. To obtain straight uniform atomically defined step-and-terrace structures, dipping in buffered HF for 45s and annealing at 1 hour at $1050°C$ where found to yield the best result. The films where confirmed epitaxial, and no relaxation was observed. But the surface is unstable resulting in 3D surfaces for thick films. Optimal film growth parameters are obtained at decreased temperature ($500°C$), delaying the critical thickness to 70nm as expected for strained, unstable epitaxial growth. The growth mode is found to be complex, commencing with 2D step-flow growth for the first 2 monolayers, before a transition to a 2D layer-by-layer growth, as the surface energy changes with STO to LSMO coverage. The layer-by-layer growth is stable until a critical thickness, but some step-bunching and roughening are observed. At the critical thickness the surface break up into a crack-like structure, where the cracks are situated at the step edges. At the interface, a strain band of 4nm is seen. I propose a model where strain is accumulated at the step-edges, leading to unstable growth. This is supported by the fact that step-bunched substrates stabilize the growth and delays the critical thickness.

The work done results in a mixed conclusion. On one hand, uniform atomically defined step-and-terrace films, as desired for applications, are obtained. On the other hand, such films are restricted by a critical thickness, which is delayed for films with a step-bunched surface structure.

The in-plane magnetic moment is measured to be $330 emu/cm^3$, a larger number than preciously recorded [1, 2], indicating ordered films. An out-of-plane component is also measured of unknown origin. No anisotropy is found in plane at room-temperature. The larger magnetic moment may be a indication that good films yields enhanced properties.

The measurements of properties in this work where only preliminary, and further research is needed to fully understand the correlation between growth and properties. In particular further magnetic measurements are needed to characterize the magnetic properties in (111)oriented films compared to other crystallographic orientations. In this respect transport measurements are essential as well. As a first case the magnetic measurements of this work should be done with respect to temperature to determine the Curie temperature and anisotropy at low temperature. The possible strain band at the interface, and domain walls/dislocations from step-edges are another aspect that needs confirmation. The role of the step-edges is still not completely understood, and the strained state of the films should be further elucidated. Is the strain at interface a result of the polar reconstructions,

structural reconstructions of the unit cell or growth parameters? It would also be interesting to see the effects of a screening layer as in [21]. For further growth studies, the control of RHEED measurements would be beneficial to enlighten the details in the growth transitions, especially at the interface. It could also be interesting to see how growth rate, pressure and laser spot area affect growth. In essence, the results of this work should be further developed to other (111)oriented systems and (111) superlattices.

References

[1] J. Fontcuberta, M. Bibes, B. Martinez, V. Trtik, C. Ferrater, F. Sanchez, and M. Varela, "Tunable epitaxial growth of magnetoresistive $la_{2/3}sr_{1/3}mno_3$ thin films," *Journal of applied physics*, vol. 85, no. 8, 1999.

[2] R. Chopdekar, E. Arenholz, and Y. Suzuki, "Orientation and thickness dependence of magnetization at the interfaces of highly spin-polarized manganite thin films," *Physical Review B*, vol. 79, no. 104417, 2009.

[3] I. Hallsteinsen, "Nanoscale domain formation in magnetic thin film oxides," December 2011.

[4] H. Kroemer, "Nobel lecture: Quasi-electric fields and band offsets: Teaching electrons new tricks," June 2012.

[5] H. Y. Hwang, Y. Iwasa, M. Kawasaki, B. Keimer, N. Nagaosa, , and Y. Tokura, "Emergent phenomena at oxide interfaces," *Nature materials*, vol. 11, 2012.

[6] L. Martin, Y.-H. Chu, and R. Rames, "Advances in the growth and characterization of magnetic, ferroelectric and multiferroic oxide thin films," *Materials Science and Engineering R*, vol. 68, pp. 89–133, 2010.

[7] P. Zubko, S. Gariglio, M. Gabay, P. Ghosez, and J. Triscone, "Interface physics in complex oxide heterostructures," *Annu. Rev, Condens. Matter Phys*, vol. 2, no. 141, pp. 141–165, 2011.

[8] C. H. Ahn, K. M. Rabe, and J.-M. Triscone, "Ferroelectricity at the nanoscale: Local polarization in oxide thin films and heterostructures," *Science*, vol. 303, no. 488, 2004.

[9] J. Chakhalian, A. J. Millis, and J. Rondinelli, "Whither the oxide interface," *Nature materials*, vol. 11, 2012.

[10] L. Li, C. Richter, J. Mannhart, and R. C. Ashoori, "Coexistence of magnetic order and two-dimensional superconductivity at $laalo_3/srtio_3$ interfaces," *Nature physics*, vol. 7, 2011.

[11] M. Konoto, T. Kohashi, K. Koike, T. Arima, Y.Kaneko, T. Tomioka, and Y. Tokura, "Magnetic domain structure of a $la_{0.7}sr_{0.3}mno_3$ (001) surface observed by a spin-polarized scanning electron microscope," *Applied physics letters*, vol. 84, no. 13, 2004.

[12] M. Cesaria, A. P. Caricato, G. Maruccioa, and M. Martino, "Lsmo - growing opportunities by pld and applications in spintronics," *Journal of Physics: Conference Series*, vol. 292, 2010.

[13] H. Boschker, J. Kautz, E. Houwman, G. Koster, and D. H. A. Blank, "Magnetic anisotropy and magnetization reversal of $la_{0.67}sr_{0.33}mno_3$ thin films on $srtio_3(110)$," *Journal of Applied Physics*, vol. 108, no. 103906, 2010.

[14] E. Dagotto, "Complexity in strongly correlated electronic systems," *Science*, vol. 309, 2005.

[15] M. Fiebig, "Revival of the magneto electric effect," *Journal of physics D: Applied physics*, vol. 38, pp. R123–R152, 2005.

[16] J. Cao and J. Wu, "Strain effects in low-dimensional transition metal oxides," *Materials Science and Engineering R*, vol. 71, 2010.

[17] A.-M. Haghiri-Gosnet and J.-P. Renard, "Cmr manganites: physics, thin films and devices," *Journal of Physics D: applied physics*, vol. 36, 2003.

[18] D. Feng and G. Jin, *Introduction to condensed matter physics 1.* World scientific publishing co., 2005.

[19] H. Johnston, "Superexchange spotted in optical lattice," December 2007.

[20] E. Eberg, *Interface effects in $PbTiO_3$ thin films and nano structures: a transmission electron microscopy study.* Thesis for the degree of philsophiae doctor, Norwegian University of Science and Technology, Department of Electronics and Telecommunications, 2011.

[21] H. Boschker, J. Verbeeck, R. Egoavil, S. Bals, G. van Tendeloo, M. Huijben, E. P. Houwman, G. Koster, D. H. A. Blank, and G. Rijnders, "Preventing the reconstruction of the polar discontinuity at oxide heterointerfaces," *Advanced functional materials*, 2012.

[22] N. Nakagawa, H. Y. Hwang, and D. A. Muller, "Why some interfaces cannot be sharp," *Nature materials*, vol. 5, 2006.

[23] M. R. Levy, *Crystal Structure and Defect Property Predictions in Ceramic Materials.* Diploma thesis, Department of Materials, Imperial College of Science, Technology and Medicine, University of London, 2005.

[24] A. Vailionis, H. Boschker, W. Siemons, E. P. Houwman, D. H. A. Blank, G. Rijnders, , and G. Koster, "Misfit strain accommodation in epitaxial abo3 perovskites: Lattice rotations and lattice modulations," *Physical Riewev B*, vol. 83, 2011.

[25] X. Hong, J.-B. Yau, J. D. Hoffman, C. H. Ahn, Y. Bason, and L. Klein, "Effect of electric field doping on the anisotropic magnetoresistance in doped manganites," *Physical review B*, vol. 74, no. 174406, 2006.

[26] G. Banach, R. Tyer, and M. Temmerman, "Study of half-metallicity in lsmo," *Journal of Magnetism and Magnetic Materials*, vol. 272-276, pp. 1963–1964, 2004.

[27] A. Khapikov, L. Uspenskaya, L. Bdkin, Y. Mukovskii, and S. Karabashec, "Magnetic domains and twin structures of the $la_{0.67}sr_{0.33}mno_3$ single crystal," *Appl. Phys. Lett.*, vol. 77, no. 2376, 2000.

[28] H. Boschker, M. Mathews, E. Houwman, H. Nishikawa, , G. Koster, and G. R. andDave H. A. Blank, "Strong uniaxial in-plane magnetic anisotropy of (001) and (011) - oriented $la_{0.67}sr_{0.33}mno_3$ thin films on $ndgao_3$ substrates," *Physical Review B*, vol. 79, no. 214425, 2009.

[29] E. Houwman, G. Maris, G. D. Luca, N. Niermann, G. Rijnders, D. Blank, and S. Speller, "Out-of-plane magnetic domain structure in a thin film of $la_{0.67}sr_{0.33}mno_3$ on $srtio_3$ (001) observed by magnetic force microscopy," *Physical review B*, vol. 77, no. 184412, 2008.

[30] D. King and D. Woodruff, *Growth and Properties of ultra thin Epitaxial Layers.* Elsevier, 1997.

[31] C. Bréchignac, P. Houdy, and M. Lahmani, *Nanomaterials and Nanochemistry.* Springer, 2007.

[32] G. Rijnders and D. H. A. Blank, "Enhanced surface diffusion through termination conversion during epitaxial $srruo_3$ growth," *Applied physics letters*, vol. 84, 2004.

[33] B. G. Orr, D. Kessler, C. W. Snyder, and L. Sander, "A model for strain-induced roughening and coherent island growth," *Europhysics letters*, vol. 19, 1992.

[34] W. H. Yang and D. J. Srolovitz, "Cracklike surface instabilities in stressed solids," *Physical review letters*, vol. 71, 1993.

[35] D. X. Huang, C. L. Chen, and A. J. Jacobson, "Interface structures and periodic film distortions induced by substrate surface steps in gd-doped ceria thin film growth," *Journal of applied physics*, vol. 97, 2005.

[36] F. Sánchez, G. Herranz, I. C. Infante, J. Fontcuberta, M. V. García-Cuenca, C. F. ande, and M. Varela, "Critical effects of substrate terraces and steps morphology on the growth mode of epitaxial srruo3 films," *Applied physics letters*, vol. 85, no. 11, 2004.

[37] F. Sanchez, I. Infante, L. Abad, U. Luders, L. Balcells, B. Martınez, and J. Fontcuberta, "Control of the surface roughening in the epitaxial growth of manganite films," *Thin solid films*, vol. 459, 2005.

[38] J. L. Blok, X. Wan, G. Koster, D. H. A. Blank, and G. Rijnders, "Epitaxial oxide growth on polar (111) surfaces," *Applied Physics Letters*, vol. 99, 2011.

[39] T.-D. Doan, J. L. Giocondi, G. S. Rohrer, and P. A. Salvador, "Surface engineering along the close-packed direction of $srtio_3$," *Journal of Crystal Growth*, vol. 225, 2001.

[40] A. Biswas, P. B. Rossen, C.-H. Yang, W. Siemons, and M.-H. Jung, "Universal ti-rich termination of atomically flat $srtio_3$ (001), (011) and (111) surfaces," *Applied Physics Letters*, vol. 98, 2011.

[41] J. Chang, Y. Park, and S. Kim, "Atomically flat single-terminated $srtio_3$ (111) surface," *Physics Letters*, vol. 92, no. 152910, 2008.

[42] H. Tanaka and T. Kawai, "Surfacestructure of reduced $srtio_3$ (111) observed by scanning tunneling microscopy," *Surface science*, vol. 365, pp. 437–442, 1996.

[43] W. Sigmund, M.Rotov, Q. Jiang, J. Brunen, J. Zegenhagen, and F. Aldinger, "A titanium-rich (111) surface of $srtio_3$ single crystals by thermal annealing," *Appl. Phys. A*, vol. 64, pp. 219–220, 1997.

[44] Y.Haruyama, Y. Aiura, H. Bando, Y. Nishihara, and H. Kato, "Annealing temperature dependence on the electronic structure of reduced $srtio_3$ (111) surface," *Journal of Electron Spectroscopy and Related Phenomena*, vol. 88-91, pp. 659–699, 1998.

[45] D. Rubi, A. Vlooswijk, and B. Noheda, "Growth of flat $srruo_3$ (111) thin films suitable as bottom electrodes in heterostructures," *Thin solid films*, vol. 517, pp. 1904–1907, 2009.

[46] J. Chang, Y.-S. Park, J.-W. Lee, and S.-K. Kim, "Layer-by-layer growth and growth-mode transition of srruo3 thin films on atomically flat single-terminated srtio3 (111) surfaces," *Journal of crystal growth*, vol. 311, 2009.

[47] D. Yongsheng, Z. Xuefeng, Y. Dunbo, and Y. Hui, "Microstructure and properties of $la_{0.7}sr_{0.3}mno_3$ films deposited on $laalo_3$ (100) , (110) , and (111) substrates," *Journal of rear earths*, vol. 24, 2006.

[48] M.-B. Lepetit, B. Mercey, , and C. Simon, "Interface effects in perovskite thin films," *Physical review letters*, vol. 108, 2012.

[49] A. Vailionis, H. Boschker, W. Siemons, E. Houwmans, and D. Blank, "Misfit strain accommodation in epitaxial abo3 perovskites; lattice rotations and lattice modulations," *Phys. Rev. B)*, vol. 83, no. 064101, pp. 1963–1964, 2011.

[50] M. Gibert, P. Zubko, R. Scherwitzl, J. Íñiguez, and J.-M. Triscone, "Exchange bias in $lanio_3$–$lamno_3$ superlattices," *Nature materials*, vol. 11, 2012.

[51] T. Ohnishi, K. Shibuya, M. Lippmaa, D. Kobayashi, H. Kumigashira, M. Oshima, and H. Koinuma, "Preparation of thermally stable tio_2-terminated $srtio_3$ (100) substrate surfaces," *Applied physics letters*, vol. 85, pp. 272–274, 2004.

[52] J. Kautz, "The structural, magnetic and electrical behavior of (110) oriented lsmo," 2009.

[53] J. E. Boschker, E. Folven, Åsmund F. Monsen, E. Wahlström, J. K. Grepstad, and T. Tybell, "Consequences of high adatom energy during pulsed laser deposition of $la_{0.7}sr_{0.3}mno_3$," *Crystal growth design*, vol. 12, 2011.

[54] J. H. Song, T. Susaki, and H. Y. Hwang, "Enhanced thermodynamic stability of epitaxial oxide thin films," *Advanced materials*, vol. 20, 2008.

[55] G. Rijnders and D. H. Blank, *Real-time Growth monitoring by High-pressure RHEED during pulsed laser deposition.* Springer, 2005.

[56] T. Kawamura and P. A. Maksym, "Origin of reflection high energy electron diffraction intensity oscillation during homoepitaxial growth on gaas(001)," *Journal of the physical society of Japan*, vol. 80, 2011.

[57] A. Fleet, D. Dale, A. R. Woll, Y. Suzuki, and J. D. Brock, "Multiple time scales in diffraction measurements of diffusive surface relaxation," *Phys. Rev. Lett.*, vol. 96, p. 055508, Feb 2006.

[58] J. E. Boschker and T. Tybell, "Qualitative determination of surface roughness by in situ reflection high energy electron diffraction," *Applied physics letters*, vol. 100, 2012.

[59] M. R. L. at UCSB, "Introduction to x-ray diffraction."

[60] S. I. Csiszár, *X-ray diffraction and X-ray absorption of strained CoO and MnO thin films.* PhD thesis, University of Groningen, 2005.

[61] A. Garg, *Growth and Characterization of Epitaxial Oxide Thin Films.* PhD thesis, University of Cambridge, 2001.

[62] M. Mathews, "Structural and magnetic properties of epitaxial la0.67sr0.33mno3 films and nanostructures," 2007.

[63] M. Birkholz, *Thin film analysis by X-ray scattering.* Wiley-vch Verlag GmbH and Co, 2006.

[64] Nanomagnetics, "Instrumentation and characterization: Vibrating sample magnetometer."

[65] K. Busxchow and F. R. Boer, *Physics of Magnetism and Magnetic materials.* Springer, 2003.

[66] H. S. Nalwa, *Handbook of Thin Film Materials.* Academic press, 2002.

[67] W. Burgei, M. J. Pechan, and H. Jaeger, "A simple vibrating sample magnetometer for use in a materials physics course," *Am. J. Phys.*, vol. 71, 2003.